8120 *Inorg. Chem.* **2009**, *48*, 8120–8133
DOI: 10.1021/ic900060d

Inorganic Chemistry
Article

Electrochemical, Linear Optical, and Nonlinear Optical Properties and Interpretation by Density Functional Theory Calculations of (4-*N,N*-Dimethylaminostyryl)-Pyridinium Pendant Group Associated with Polypyridinic Ligands and Respective Multifunctional Metal Complexes (Ru^{II} or Zn^{II})

Frédéric Dumur,[†] Cédric R. Mayer,*[,†] Khuyen Hoang-Thi,[‡] Isabelle Ledoux-Rak,[‡] Fabien Miomandre,[‡] Gilles Clavier,[‡] Eddy Dumas,[†] Rachel Méallet-Renault,[‡] Michel Frigoli,[†] Joseph Zyss,[‡] and Francis Sécheresse[†]

[†]*Institut Lavoisier de Versailles, UMR-CNRS 8180, Université de Versailles Saint-Quentin-en-Yvelines, 78035 Versailles, France, and* [‡]*Institut d'Alembert, IFR 121, Ecole Normale Supérieure de Cachan, 94235 Cachan, France*

Received January 13, 2009

The synthesis, linear optical and nonlinear optical properties, as well as the electrochemical behavior of a series of pro-ligands containing the 4-(4-*N,N*-dimethylaminostyryl)-1-methyl pyridinium (*DASP*$^+$) group as a push−pull moiety covalently linked to terpyridine or bipyridine as chelating ligands are reported in this full paper. The corresponding multifunctional Ru^{II} and Zn^{II} complexes were prepared and investigated. The structural, electronic, and optical properties of the pro-ligands and the ruthenium complexes were investigated using density functional theory (DFT) and time-dependent (TD) DFT calculations. A fairly good agreement was observed between the experimental and the calculated electronic spectra of the pro-ligands and their corresponding ruthenium complexes. A quenching of luminescence was evidenced in all ruthenium complexes compared with the free pro-ligands but even the terpyridine-functionalized metal complexes exhibited detectable luminescence at room temperature. Second order nonlinear optical (NLO) measurements were performed by Harmonic Light Scattering and the contribution of the *DASP*$^+$ moieties (and their relative ordering) and the metal-polypyridyl core need to be considered to explain the nonlinear optical properties of the metal complexes.

Introduction

Molecular push−pull materials which exhibit electrochemical and optical (linear and nonlinear) properties are of great current interest because of their potential utility in telecommunications, optical data storage, and novel optoelectronic technologies.[1,2] Stilbazolium like dyes have been the topic of many studies in these fields. Modification of the dyes is one of the essential strategies to improve electrochemical, optical, and nonlinear optical (second harmonic generation) properties. These chromophores, on the basis of a push−pull system, consist of an electron donating group (*D*) and an electron withdrawing group (*A*) coupled through a π-conjugated spacer. The molecular properties of the chromophores depend on the strength of the push−pull effects which are a function of the ability of the donor to provide electrons and the acceptor to withdraw electrons. Concerning pure organic chromophores exhibiting intense nonlinear optical (NLO) response, *N,N*-dimethylaniline has been widely studied as a donating group in push−pull molecules.[3−5] In the solid state, organic crystals of 4-(4-*N,N*-dimethylaminostyryl)-1-methyl pyridinium tosylate (*DAST*) have one of the largest NLO coefficient among organic materials.[6] In addition, this class of organic materials has been investigated for two-photon pumped up-conversion lasing properties[7] and has also been used as fluorescent probe for

*To whom correspondence should be addressed. E-mail: cmayer@chimie.uvsq.fr. Fax: (+) 33 1 39 25 43 81. Phone: (+) 33 1 39 25 43 80.

(1) Zyss, J.; *Molecular Nonlinear Optics: Materials, Physics and Devices*; Academic Press: Boston, 1994.
(2) *Nonlinear Optics of Organic Molecules and Polymers*; Nalwa, H. S., Miyara, S., Eds.; CRC Press: Boca Raton, FL, 1997.
(3) Roberto, D.; Ugo, R.; Bruni, S.; Cariati, E.; Cariati, F.; Fantucci, P.; Invernizzi, I.; Quici, S.; Ledoux, I.; Zyss, J. *Organometallics* **2000**, *19*, 1775–1788.
(4) Coe, B. J.; Harris, J. A.; Asselberghs, I.; Wostyn, K.; Clays, K.; Persoons, A.; Brunschwig, B. S.; Coles, S. J.; Gelbrich, T.; Light, M. E.; Hursthouse, M. B.; Nakatani, K. *Adv. Funct. Mater.* **2003**, *13*, 347–357.
(5) Dumur, F.; Mayer, C. R.; Dumas, E.; Miomandre, F.; Frigoli, M.; Sécheresse, F. *Org. Lett.* **2008**, *10*, 321–324.
(6) Lee, K. S.; Kim, O.-K. *Photonics Sci. News* **1999**, *4*, 9–20.
(7) Ren, Y.; Fang, Q.; Yu, W.-T.; Tian, Y.-P.; Jiang, M.-H.; Yang, Q.-C.; Mak, T. C. W. *J. Mater. Chem.* **2000**, *10*, 2025–2030.

Published on Web 07/30/2009

cell microviscosity[8] or sensitizer for the photodynamic therapy of cancer.[9]

Parallel to this area, the chemistry of metallic complexes based on ruthenium(II) and polypyridyl ligands constitutes a vast field of research with applications ranging from antitumoral activity[10] to electronic devices,[11] and optical (linear and nonlinear) properties.[12−17] The most studied complexes based on ruthenium are derived from the well-known Ru^{II}-tris-bipyridine complex. The main interest in bipyridine-metal complexes lies on their luminescence properties which can be observed at room temperature.[18] However, all polypyridyl ruthenium(II) complexes do not exhibit photoluminescence at room temperature, and some of them give measurable emission states only at low temperature, which is indeed a limiting factor for a variety of applications. Ruthenium complexes made of terpyridine as ligand correspond to this category. However, Hanan et al. have shown a counterexample by substituting terpyridine ligands of Ru^{II}-bis-terpyridine by tridentate ligands based on the 2-aryl-4,6-bis(2-pyridyl)-*s*-triazine motif.[19] The strategy developed in that specific case was based on the removal of the protons of the central pyridine unit of the terpyridine. The synthesis of these tridentate ligands generated a coplanar arrangement of the rings resulting in a detectable luminescence at room temperature.

Polypyridyl metal complexes have also been used to generate push−pull systems. Many studies are devoted to the functionalization of chelating ligands by appropriate organic electron donors. Hauser et al. recently described the synthesis of an annulated donor−acceptor (D-A) ensemble, combining the strong electron donor tetrathiafulvalene (TTF) with a phenanthroline group. This pro-ligand was further used to obtain ruthenium(II) complexes exhibiting a long-lived ligand-to-ligand charge separated (LLCS) state at room temperature.[20,21] It has to be noticed that the push−pull system is often only induced by coordination of the chelating group to a metal center. Several examples have been reported with bipyridine[12−15] and terpyridine[22−26] as chelating fragments. Different research groups have also reported the use of the *N,N*-dimethylaminostyrylpyridine moiety directly coordinated to a metal to induce either quadratic hyperpolarizability properties,[27] to control the absorbance and luminescence properties of the resulting complexes,[28] or to realize photovoltaic devices.[29]

Our research group is involved in the design and investigation of metal complexes for the conception of nanocomposites exhibiting electrochemical properties and photoluminescence at room temperature.[30] Here, we report on the preparation and properties of three pro-ligands $\mathbf{L_1}$−$\mathbf{L_3}$ containing the well-known 4-(4-*N,N*-dimethylaminostyryl)-1-methyl pyridinium ($DASP^+$) chromophore linked to the chelating fragment via a methylene group, as seen in Scheme 1.

One chromophore ($\mathbf{L_1}$) or two chromophores ($\mathbf{L_2}$, $\mathbf{L_3}$) have been attached to the chelating fragment. We mostly focused on terpyridinic pro-ligands because of their specific topology that can lead to metallowires for the functionalization of metallic surfaces[31] and because of their "facile" 4′-functionalization for the synthesis of star-shape ligands,[32,33] metallomacrocycles, or metallopolymers.[34−36] Six metal complexes were synthesized with these pro-ligands upon coordination with Zn^{II} or Ru^{II} as metal cations (Scheme 2). For each metal center, one homoleptic $[M(\mathbf{L_1})_2]^{4+}$ (**Ru-1** and **Zn-1**) and one heteroleptic $[M(\mathbf{L_1})$(4′-(4-*N,N*-dimethylamino phenyl)-2,2′:6′,2″-terpyridine)$]^{3+}$ (**Ru-1′** and **Zn-1′**) complex were prepared. $[Ru(\mathbf{L_2})_2]^{6+}$ (**Ru-2**) contains a total of four $DASP^+$ moieties while $[Ru(bpy)_2(\mathbf{L_3})]^{4+}$ (**Ru-3**) was specifically designed to study the electronic impact of the dye on the Ru^{II}-tris-bipyridine complex (Scheme 2). The absorption and luminescence properties were studied for all ligands and complexes. We also analyzed the second order NLO properties of several complexes by using Harmonic Light Scattering (HLS) technique at 1.64 μm. Finally, the experimental optoelectrochemical properties were compared to theoretical studies realized by Density Functional Theory (DFT) calculations.

Experimental Section

Chemicals. All reagents and solvents were purchased from Aldrich and used without further purification. Intermediates

(8) Wandelt, B.; Mielniczak, A.; Turkewitsch, P.; Darling, G. D.; Stranix, B. R. *Biosens. Bioelectron.* **2003**, *18*, 465–471.
(9) Leonard, K. A.; Nelen, M. I.; Simard, T. P.; Davies, S. R.; Gollnick, S. O.; Oseroff, A. R.; Gibson, S. L.; Hilf, R.; Chen, L. B.; Detty, M. R. J. *Med. Chem.* **1999**, *42*, 3953–3964.
(10) Erkkila, K. E.; Odom, D. T.; Barton, J. K. *Chem. Rev.* **1999**, *99*, 2777–2795.
(11) Balzani, V.; Moggi, L.; Scandola, F. *Supramolecular photochemistry*; Balzani, V., Ed.; Reidel: Dordrecht, The Netherlands, 1987.
(12) Le Bouder, T.; Maury, O.; Bondon, A.; Costuas, K.; Amouyal, E.; Zyss, I.; Le Bozec, H. *J. Am. Chem. Soc.* **2003**, *125*, 12284–12299.
(13) Dhenaut, C.; Ledoux, I.; Samuel, I. D. W.; Zyss, J.; Bourgault, M.; Le Bozec, H. *Nature* **1995**, *374*, 339–342.
(14) Le Bozec, H.; Renouard, T.; Bourgault, M.; Dhenaut, C.; Brasselet, S.; Ledoux, I.; Zyss, J. *Synth. Met.* **2001**, *124*, 185–189.
(15) Morrison, I. D.; Denning, R. G.; Laidlaw, W. M.; Stammers, M. A. *Rev. Sci. Instrum.* **1996**, *67*, 1445–1453.
(16) Coe, B. J.; Harris, J. A.; Brunschwig, B. S.; Asselberghs, I.; Clays, K.; Garín, J.; Orduna, J. *J. Am. Chem. Soc.* **2005**, *127*, 13399–13410.
(17) Vance, F. W.; Hupp, J. T. *J. Am. Chem. Soc.* **1999**, *121*, 4047–4053.
(18) See for example: Glazer, E. C.; Magde, D.; Tor, Y. *J. Am. Chem. Soc.* **2007**, *129*, 8544–8551.
(19) Polson, M. I. J.; Medlycott, E. A.; Hanan, G. S.; Mikelsons, L.; Tayor, N. J.; Watanabe, M.; Tanake, Y.; Loiseau, F.; Passalcqua, R.; Campagna, S. *Chem.—Eur. J.* **2004**, *10*, 3640–3648.
(20) Jia, C.; Liu, S.-X.; Tanner, C.; Leiggener, C.; Neels, A.; Sanguinet, L.; Levillain, E.; Leutwyler, S.; Hauser, A.; Decurtins, S. *Chem.—Eur. J.* **2007**, *13*, 3804–3812.
(21) Goze, C.; Leiggener, C.; Liu, S.-X.; Sanguinet, L.; Levillain, E.; Hauser, A.; Decurtins, S. *ChemPhysChem* **2007**, *8*, 1504–1512.
(22) Tessore, F.; Roberto, D.; Ugo, R.; Pizzotti, M.; Quici, S.; Cavazzini, M.; Bruni, S.; De Angelis, F. *Inorg. Chem.* **2005**, *44*, 8967–8978.
(23) Roberto, D.; Tessore, F.; Ugo, R.; Bruni, S.; Manfredi, A.; Quici, S. *Chem. Commun.* **2002**, 846–847.
(24) Duncan, T. V.; Song, K.; Hung, S.-T.; Miloradovic, I.; Nayak, A.; Persoons, A.; Verbiest, T.; Therien, M. J.; Clays, K. *Angew. Chem., Int. Ed.* **2008**, *47*, 2978–2981.
(25) Uyeda, H. T.; Zhao, Y.; Wostyn, K.; Asselberghs, I.; Clays, K.; Persoons, A.; Therien, M. J. *J. Am. Chem. Soc.* **2002**, *124*, 13806–13813.
(26) De Angelis, F.; Fantacci, S.; Sgamelotti, A.; Cariati, F.; Roberto, D.; Tessore, F.; Ugo, R. *Dalton Trans.* **2006**, 852–859.
(27) Lucenti, E.; Cariati, E.; Dragonetti, C.; Manassero, L.; Tessore, F. *Organometallics* **2004**, *23*, 687–692.
(28) Cariati, E.; Roberto, D.; Ugo, R.; Ford, P. C.; Galli, S.; Sironi, A. *Inorg. Chem.* **2005**, *44*, 4077–4085.
(29) Jang, S.-R.; Lee, C.; Choi, H.; Ko, J. J.; Lee, J.; Vittal, R.; Kim, K.-J. *Chem. Mater.* **2006**, *18*, 5604–5608.
(30) Mayer, C. R.; Dumas, E.; Miomandre, F.; Méallet-Renault, R.; Warmont, F.; Vigneron, J.; Etcheberry, A.; Sécheresse, F. *New. J. Chem.* **2006**, *30*, 1628–1637.
(31) Maskus, M.; Abruña, H. D. *Langmuir* **1996**, *12*, 4455–4462.
(32) Dumur, F.; Mayer, C. R.; Dumas, E.; Sécheresse, F. *Tetrahedron Lett.* **2007**, *48*, 4143–4146.
(33) Mayer, C. R.; Dumur, F.; Miomandre, F.; Dumas, E.; Devic, T.; Fosse, C.; Sécheresse, F. *New J. Chem.* **2007**, 1806–1814.
(34) Constable, E. C. *Chem. Soc. Rev.* **2007**, *36*, 246–253.
(35) Hofmeier, H.; Schubert, U. S. *Chem. Soc. Rev.* **2004**, *33*, 373–399.
(36) Andres, P. R.; Schubert, U. S. *Adv. Mater.* **2004**, *16*, 1043–1068.

Scheme 1. Structures of Pro-Ligands L_1, L_2, and L_3

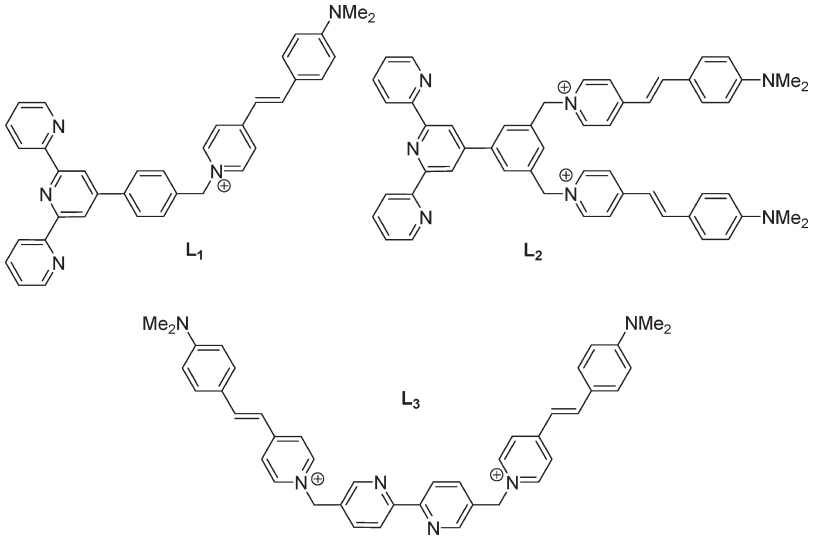

Scheme 2. Structures of Complexes **M-1**, **M-1′** (with M = Ru, Zn), **Ru-2** and **Ru-3**

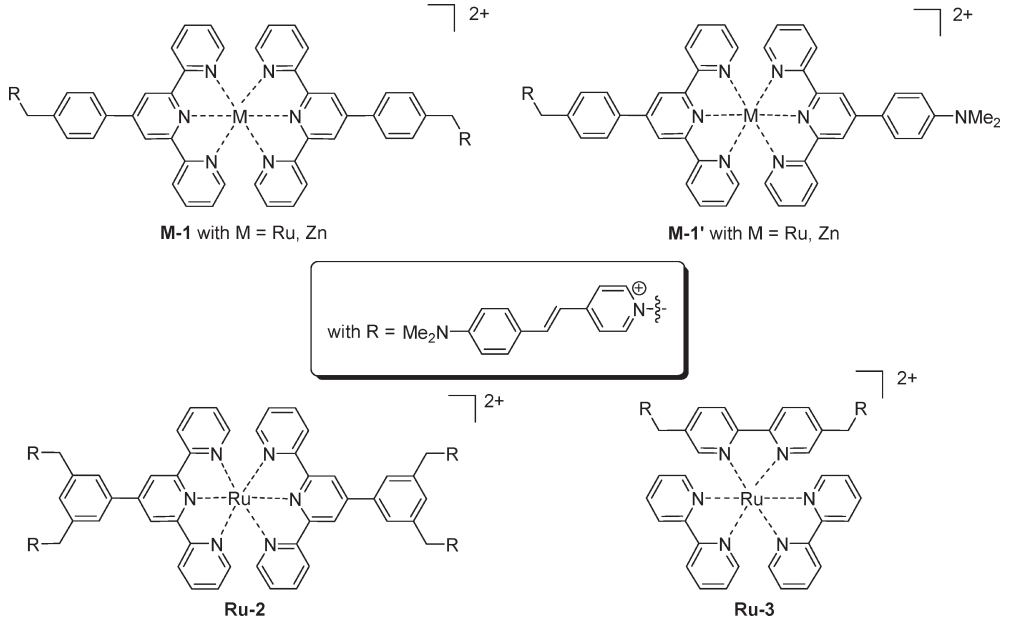

4-dimethylaminostyryl-4-pyridine (*DASpyr*),[37] *trans*-4′-(dimethylamino)-*N*-methyl-4-stilbazolium hexafluorophosphate (Me-*DASP*·PF_6),[38] 4′-(4-bromomethylphenyl)-2,2′,6′,2″-terpyridine (tpy-CH_2Br),[39] 4′-(4-dimethylamino-phenyl)-2,2′:6′,2″-terpyridine (tpy-NMe_2),[13] 4′-(3,5-di(bromomethyl)-phenyl)-2,2′,6′,2″-terpyridine (tpy-$(CH_2Br)_2$),[40] 5,5′-di(bromomethyl)-2,2′-bipyridine (bpy-$(CH_2Br)_2$),[41] and $[(bpy)_2RuCl_2]$[42] were synthesized following the procedures previously reported in the literature, without modification and with similar yields.

Instrumentation and Methods. ESI-MS measurements were carried out with an API 3000 (ESI/MS/MS) PE-SCIEX triple quadrupole mass spectrometer and a HP 5989B single quadrupole mass spectrometer equipped with an electrospray source from Analytica of Branford. Both instruments were operated in the positive ion mode. For the API 3000 (ESI/MS/MS) PE SCIEX triple quadrupole mass spectrometer, the experiments were performed either by direct infusion with a syringe pump with flow rate of 10 μL min^{-1} or by flow injection acquisition with flow rate of 200 μL.min^{-1}. Standard experimental conditions were as follows: sample concentration 10^{-3} to 10^{-5} M; nebulizing gas N_2, 7 units flow rate on a range of 10; ion spray voltage, −5.00 kV; temperature, 200−400 °C; declustering potential, −20 V; focusing potential, −200 V; entrance potential, 10 V. UV−visible absorption spectra before luminescence analysis were measured with a Varian CARY 500 spectrophotometer from 280 to 800 nm. Emission spectra were measured on a SPEX Fluoromax-3 (Jobin-Yvon), upon excitation wavelength at 469 nm. All solvents were of spectroscopic grade. Optical density was adjusted below 0.1 to avoid reabsorption

(37) Pepitone, M. F.; Jernigan, G. G.; Melinger, J. S.; Kim, O.-K. *Org. Lett*. **2007**, *9*, 801–804.
(38) Huang, Y.; Cheng, T.; Li, F.; Huang, C.-H.; Hou, T.; Yu, A.; Zhao, X.; Xu, X. *J. Phys. Chem. B*. **2002**, *106*, 10020–10030.
(39) Yuan, S.-C.; Chen, H.-B.; Zhang, Y.; Pei, J. *Org. Lett*. **2006**, *8*, 5701–5704.
(40) Gagliardo, M.; Perelaer, J.; Hartl, F.; van Klink, G. P. M.; van Koten, G. *Eur. J. Inorg. Chem*. **2007**, 2111–2120.
(41) Peng, Z.; Gharavi, A. R.; Yu, L. *J. Am. Chem. Soc*. **1997**, *119*, 4622–4632.
(42) Sullivan, B. P.; Salmon, D. J.; Meyer, T. J. *Inorg. Chem*. **1989**, *17*, 3334–3336.

artifacts. $[Ru(bpy)_2(dmb)].(PF_6)_2$ (dmb = 4,4′-dimethylbipyridine) in acetonitrile was used as the reference for the measurements of luminescence quantum yields. ^1H and ^{13}C NMR spectra were recorded at room temperature in 5 mm o.d. tubes on a Bruker Avance 300 spectrometer equipped with a QNP probe head. Elemental analyses were performed by the "Service Central d'Analyse du CNRS", Vernaison (France). All calculations were performed with the Gaussian03 program[43] in vacuo on a Nec TX7 with 32 processors Itanium 2 of the MESO center of the ENS Cachan. Orbitals were generated with the cubgen module of Gaussian and visualized with GaussView 3.0 of Gaussian Inc. GaussSum 2.1[44] was used for the electronic spectrum simulation. The equation employed by the program to calculate the theoretical spectrum and the extinction coefficients is based on Gaussian convolution and is reported in the open source code of the program (available at http://gausssum.svn.sf.net/viewvc/gausssum/Trunk/src/gausssum/). The full width at half-maximum value used for the simulated spectrum was 2800 cm^{-1}. The accuracy of the theoretical method concerning the energy of the various electronic transitions was reflected by the energy of the resulting simulated absorption bands at their maximum (E^{max}_{calcd}) as compared to the corresponding experimental band maxima (E^{max}_{expt}). This mismatch was quantified via a reliability factor, R (%), as follows:

$$R = \frac{E^{max}_{calcd} - E^{max}_{expt}}{E^{max}_{expt}} \times 100$$

Electrochemical measurements were performed in a three electrode cell equipped with a 1 mm diameter platinum disk as the working electrode, platinum wire as the counter electrode, and Ag^+ (0.01 M)/Ag as the reference electrode. The reference potential was checked versus ferrocene as recommended by IUPAC ($E°$_Fc = +86 mV).[45] The supporting electrolyte was tetrabutylammonium hexafluorophosphate (Fluka, puriss.), and the solutions were deaerated by argon bubbling prior each experiment. Cyclic voltammograms (CVs) were recorded with a 600 CH Instruments potentiostat connected to a PC.

In the present work, hyperpolarizability (β) measurements have been made using the HLS technique[46,47] at λ = 1640 nm as the fundamental wavelength. Concentrated solutions ($> 10^{-3}$ mol L^{-1}) of molecules with large expected β values ($> 5 \times 10^{-28}$ esu) are used in the near-IR harmonic wavelength range at 1640 nm, as both scattering intensity and detector sensitivity are much lower at the 820 nm harmonic wavelength than in the visible. The 1640 nm fundamental beam is emitted by an optical parametric oscillator (OPO) from GWU (VersaScan/170) pumped at 355 nm by a frequency-tripled Nd^{3+}:YAG nanosecond laser (SAGA from Thales Laser) at a 10 Hz repetition rate. The typical energy per pulse at 1640 nm is 7 mJ. The intensity of the incoming fundamental beam is varied using a half-wave plate rotated between two crossed polarizers. HLS photons at 820 nm are focused onto the PMT using two collecting lenses. The detected signal is then sampled and averaged using a Boxcar and processed by a computer. A low intensity reference beam is extracted from the main beam at a 45° incidence angle by a glass plate and focused onto a highly nonlinear NPP (*N*-4-nitrophenyl-prolinol) powder used as a frequency doubler.[48] The variation of the scattered second harmonic intensity from the solution is recorded on the computer as a function of the reference second harmonic signal provided by the NPP powder. β values are then inferred from the slopes of the resulting lines.

Our reference sample is a concentrated (1.15×10^{-2} mol L^{-1}) solution of Ethyl Violet (EtV). Its octupolar β value is 230×10^{-30} esu at 1640 nm, a value inferred from β measured at 1900 nm[49] using a two-level dispersion model.[50] The intensity of the harmonic scattered light from a solution with N molecules per cm^3 of solute and N_S molecules per cm^3 of solvent is given by $I^{2w} = G(N_S\langle\beta_S{}^2\rangle + N\langle\beta^2\rangle)(I^{\omega})^2$ where $\langle\beta^2\rangle$ is the orientational average of the tensor product $\beta\otimes\beta$ of the second-order hyperpolarizability of the solvent (β_S) or the solute (β), I^{ω} is the intensity of incident radiation, and G a coefficient including geometrical factors, local field factors, and other experimental correction terms. In the present case, the $N_S\langle\beta_S{}^2\rangle$ term is negligible with respect to $N\langle\beta^2\rangle$; as a consequence, $\langle\beta^2\rangle$ is simply inferred from the ratio between the slope of the sample (p) and that of the Ethyl Violet solution $(p_{EtV})\langle\beta^2\rangle = \frac{N_{EtV}p}{Np_{EtV}}\langle\beta_{EtV}{}^2\rangle$

According to most NLO studies using HLS, we will report as "β" values the square root of $\langle\beta^2\rangle$,[51] given in esu.

4′-{4-(4-Dimethylaminostyryl-4-pyridiniumyl)methyl}-2,2′:6′,2″-terpyridine bromide ($L_1 \cdot Br$). *DASpyr* (0.74 g, 3.3 mmol) and tpy-CH_2Br (1.2 g, 3 mmol) were solubilized in acetonitrile (120 mL) and stirred at reflux for one night. The resulting red solution was partially concentrated, and the pure product was precipitated by slow addition of diethyl ether. The ligand was recovered by filtration, washed several times with ether, and dried in vacuum. (Yield, 1.6 g, 85%).

^1H NMR (DMSO-d_6), δ ppm: 8.98 (d, 2H, ^3J = 6.3 Hz), 8.75 (d, 2H, ^3J = 3.9 Hz), 8.68 (s, 2H), 8.66 (d, 2H, ^3J = 12.1 Hz), 8.11 (d, 1H, ^3J = 6.3 Hz), 7.95−8.05 (m, 6H), 7.72 (d, 2H, ^3J = 7.6 Hz), 7.59 (d, 2H, ^3J = 8.4 Hz), 7.52 (t, 2H, ^3J = 5.5 Hz), 7.18 (d, 1H, ^3J = 15.9 Hz), 6.75 (d, 2H, ^3J = 8.6 Hz), 5.81 (s, 2H, $-CH_2$-py$^+$), 3.00 (s, 6H, NMe_2). ^{13}C NMR (75.47 MHz, DMSO-d_6), δ ppm: 39.7, 61.1, 111.2, 116.9, 118.0, 121.0, 122.4, 122.7, 124.6, 127.7, 129.5, 130.3, 136.0, 137.6, 138.1, 142.7, 143.6, 148.7, 149.2, 151.9, 154.2, 154.7, 155.6. UV−visible (CH_3CN) [λ_{max} (nm); (ε_{max}) (M^{-1} cm^{-1})]: 485 (33420), 272 (77670). ESI Mass Spectrum (m/z) (positive mode): 546.3 [$C_{37}H_{32}N_5{}^+$]. Anal. Found: C, 70.89; H, 5.12; N, 11.09; Br, 12.86. Calcd for $C_{37}H_{32}N_5Br$ (%): C, 70.92; H, 5.15; N, 11.18; Br, 12.75.

$L_1 \cdot (PF_6)$. The hexafluorophosphate salt of L_1 was prepared by addition of a concentrated aqueous solution of $NaPF_6$ to an aqueous solution of $L_1 \cdot Br$. The hexafluorophosphate salt precipitated and was recovered by filtration, dried with diethyl ether and used without further purification.

4′-(3,5-Bis{[4-dimethylaminostyryl-4-pyridiniumyl]methyl})-2,2′:6′,2″-terpyridine hexafluorophosphate ($L_2 \cdot (PF_6)_2$). L_2 was synthesized starting from *DASpyr* (0.905 g, 4 mmol) and tpy-$(CH_2Br)_2$ (1 g, 2 mmol) using the procedure described for the synthesis of L_1. Acetonitrile was partially evaporated, and the product precipitated by addition of a concentrated aqueous solution of sodium hexafluorophosphate. The precipitate was filtered. The crude product was then dissolved in acetonitrile, and precipitated by slow addition of ether. L_2 was finally filtered and dried in vacuum (Yield, 1.24 g, 79%).

^1H NMR (DMSO-d_6), δ ppm: 8.98 (d, 4H, ^3J = 6.55 Hz), 8.83 (s, 2H), 8.80 (d, 2H, ^3J = 4.05 Hz), 8.73 (d, 2H, ^3J = 7.9 Hz), 8.30 (d, 2H, ^4J = 1.3 Hz), 8.10 (m, 8H), 7.96 (d, 2H, ^3J = 16 Hz), 7.79 (t, 1H, ^4J = 1.3 Hz), 7.58 (d, 4H, ^3J = 8.7 Hz), 7.20 (d, 2H, ^3J = 16 Hz), 6.77 (d, 4H, ^3J = 8.7 Hz), 5.80 (s, 4H, $-CH_2$-py$^+$), 3.02 (s, 12H, N$-CH_3$). ^{13}C NMR (75.47 MHz, DMSO-d_6), δ ppm: 39.7, 60.7, 111.3, 117.1, 117.9, 121.1, 122.4, 122.8, 125.3,

(43) Frisch, M. et al. *Gaussian 03*, revision D0.1; Gaussian Inc.: Wallingford, CT, 2004 (full reference given in the Supporting Information).
(44) (a) O'Boyle, N. M.; Tenderholt, A. L.; Langner, K. M. *J. Comput. Chem.* **2008**, *29*, 839–845. (b) O'Boyle, N. M.; Vos, J. G. *GaussSum*, version 2.1; Dublin City University: Dublin, Ireland, 2007; available at http://gausssum.sourceforge.net.
(45) Gritzner, G.; Kuta, J. *Pure Appl. Chem.* **1984**, *56*, 461–466.
(46) Terhune, R. W.; Maker, P. D.; Savage, C. M. *Phys. Rev. Lett.* **1965**, *14*, 681–684.
(47) Clays, K.; Persoons, A. *Phys. Rev. Lett.* **1991**, *66*, 2980–2983.
(48) Zyss, J.; Nicoud, J. F.; Coquillay, M. *J. Chem. Phys.* **1984**, *81*, 4160–4167.
(49) Le Bozec, H.; Le Bouder, T.; Maury, O.; Bondon, A.; Ledoux, I.; Deveau, S.; Zyss, J. *Adv. Mater.* **2001**, *22*, 1677–1681.
(50) Oudar, J. L. *J. Chem. Phys.* **1977**, *67*, 446–457.
(51) Russier-Antoine, I.; Huang, J.; Benichou, E.; Bachelier, G.; Jonin, C.; Brevet, P. F. *Chem. Phys. Lett.* **2008**, *450*, 345–349.

127.6, 129.8, 130.3, 136.1, 137.5, 138.3, 143.1, 143.8, 148.6, 149.2, 152.4, 154.6, 155.3, 155.7. UV−visible (CH_3CN) [λ_{max} (nm); (ε_{max}) (M^{-1} cm^{-1})]: 485 (65370), 274 (35410) . ESI Mass Spectrum (m/z) (positive mode): 391.9 ($[C_{53}H_{49}N_7]^{2+}/2$); Anal. Found: C, 59.34; H, 4.73; N, 9.17; P, 5.71; F, 21.18. Calcd for $C_{53}H_{49}N_7P_2F_{12}$ (%): C, 59.27; H, 4.60; N, 9.13; P, 5.77; F, 21.23.

$L_2 \cdot Cl_2$. The chloride salt of L_2 was prepared by addition of tetrabutylammonium chloride to a solution of $L_2 \cdot (PF_6)_2$ in acetone. $L_2 \cdot Cl_2$ precipitated and was recovered by filtration, dried with diethyl ether, and used without further purification.

5,5′-Di([4-dimethylaminostyryl-4-pyridiniumyl]methyl)-2,2′-bipyridine hexafluorophosphate ($L_3 \cdot (PF_6)_2$). Ligand L_3 was synthesized and purified according to the procedure used for L_2 starting from *DASpyr* (0.905 g, 4 mmol) and *bpy*-$(CH_2Br)_2$ (684 mg, 2 mmol) (Yield, 1.7 g, 93%).

^{1}H NMR (DMSO-d_6), δ ppm: 8.96 (d, 4H, ^3J = 6.55 Hz), 8.90 (d, 2H, ^3J = 1.3 Hz), 8.44 (d, 2H, ^3J = 8.9 Hz), 8.10 (d, 4H, ^3J = 6.55 Hz), 8.08 (d, 2H, ^3J = 1.3 Hz), 7.96 (d, 2H, ^3J = 16 Hz), 7.60 (d, 4H, ^3J = 8.9 Hz), 7.20 (d, 2H, ^3J = 16 Hz), 6.79 (d, 4H, ^3J = 8.9 Hz), 5.81 (s, 4H, $-CH_2$-py$^+$), 3.02 (s, 12H, N$-CH_3$). ^{13}C NMR (75.47 MHz, DMSO-d_6), δ ppm: 39.7, 58.9, 111.9, 116.9, 118.2, 120.8, 122.3, 122.7, 124.7, 127.8, 129.2, 130.4, 136.2, 137.7, 138.0, 142.8, 143.6, 148.8, 149.6, 152.0, 154.4, 154.9, 156.1. UV−visible (CH_3CN) [λ_{max} (nm); (ε_{max}) (M^{-1} cm^{-1})]: 486 (78120), 287 (29510). ESI Mass Spectrum (m/z) (positive mode): 315.5 ($[C_{42}H_{42}N_6]^{2+}/2$). Anal. Found: C, 54.68; H, 4.57; N, 9.06; P, 6.92; F, 24.85. Calcd for $C_{42}H_{42}N_6P_2F_{12}$ (%): C, 54.79; H, 4.60; N, 9.13; P, 6.73; F, 24.76.

$[Ru(L_1)Cl_3] \cdot Cl$. $RuCl_3 \cdot 3H_20$ (0.785 g, 3 mmol) was dissolved in ethanol (45 mL). A solution of $L_1 \cdot Br$ (0.941 g, 1.5 mmol) in ethanol (40 mL) was added dropwise, and the mixture was stirred at reflux for one night. The resulting mixture was filtrated while hot. The precipitate was vigorously washed with water (3 × 20 mL), ethanol (1 × 20 mL), and diethyl ether (2 × 20 mL). $[Ru(L_1)Cl_3] \cdot Cl$ was dried overnight in a vacuum desiccator over P_2O_5 (Yield, 1.14 g, 96%).

Anal. Found: C, 56.13; H, 4.01; N, 8.69; Cl, 18.11; Ru, 12.64. Calcd for $C_{37}H_{32}Cl_4N_5Ru$ (%): C, 56.28; H, 4.09; N, 8.87; Cl, 17.96; Ru, 12.80.

$[Ru(L_2)Cl_3] \cdot Cl_2$. $[Ru(L_2)Cl_3] \cdot Cl_2$ was synthesized according to the above-described procedure for $[Ru(L_1)Cl_3] \cdot Cl$ using $RuCl_3 \cdot 3H_20$ (0.393 g, 1.5 mmol) and $L_2 \cdot Cl_2$ (0.650 g, 0.75 mmol). (Yield, 0.693 g, 87%).

Anal. Found: C, 59.79; H, 4.57; N, 9.14; Cl, 16.88; Ru, 9.43. Calcd for $C_{53}H_{49}Cl_5N_7Ru$ (%): C, 59.92; H, 4.65; N, 9.23; Cl, 16.69; Ru, 9.51.

$[Zn(L_1)Cl_3]$. $ZnCl_2 \cdot 2H_20$ (0.517 g, 3 mmol) was dissolved in ethanol (20 mL). A solution of $L_1 \cdot Br$ (0.941 g, 1.5 mmol) in ethanol (40 mL) was added to the previous solution, and the resulting mixture was stirred at reflux for 3 h. The mixture was filtrated while hot, and the precipitate was vigorously washed with ethanol (3 × 20 mL) and diethyl ether (2 × 20 mL). The product was dried under vacuum over P_2O_5 (Yield, 1 g, 93%).

Anal. Found: C, 61.57; H, 4.41; N, 9.63; Zn, 9.02; Cl, 14.93. Calcd for $C_{37}H_{32}N_5ZnCl_3$ (%): C, 61.86; H, 4.49; N, 9.75; Zn, 9.10; Cl, 14.80.

$[Ru(L_1)_2] \cdot (PF_6)_4$ - (Ru-1). $[Ru(L_1)Cl_3] \cdot Cl$ (0.079 g, 0.1 mmol) and $L_1 \cdot Br$ (0.063 g, 0.1 mmol) were refluxed overnight in a mixture of EtOH/H_2O/DMF (45/15/3 mL). The mixture was cooled to room temperature, and an aqueous solution of NH_4PF_6 (0.200 g, 5 mL) was added. The resulting mixture was concentrated under vacuum to about 25 mL, and 80 mL of water were added. The dark-red solid was filtered and washed successively with water (3 × 10 mL), ethanol (3 × 10 mL), and diethyl ether (3 × 10 mL). Then, the crude product was purified by flash column chromatography (R_f = 0.4, Al_2O_3, sat. aq. KNO_3/CH_3CN: 5/95). The eluted solution was concentrated under reduced pressure. The purified complex (which is constituted of a mixture of hexafluorophosphate and potassium salts) was isolated as a dark-red solid by precipitation with a concentrated solution of NH_4PF_6, washed with ethanol (2 × 10 mL), and dried with diethyl ether (2 × 10 mL). (Yield, 0.091 g, 51%).

^{1}H NMR (DMSO-d_6), δ ppm: 9.48 (s, 4H), 9.07 (d, 4H, ^3J = 8.3 Hz), 9.00 (d, 4H, ^3J = 6.7 Hz), 8.50 (d, 4H, ^3J = 8.1 Hz), 8.16 (d, 4H, ^3J = 6.6 Hz), 8.10 (t, 4H, ^3J = 7.5 Hz), 7.99 (d, 4H, ^3J = 16 Hz), 7.91 (d, 4H, ^3J = 8.1 Hz), 7.63 (d, 4H, ^3J = 8.7 Hz), 7.52 (d, 4H, ^3J = 8.9 Hz), 7.28 (dd, 4H, ^3J = 6.2 Hz), 6.81 (d, 4H, ^3J = 9 Hz), 5.84 (s, 4H, $-CH_2$-py$^+$), 3.04 (s, 12H, N$-CH_3$). UV−visible (CH_3CN) [λ_{max} (nm); (ε_{max}) (M^{-1} cm^{-1})]: 493 (71780), 310 (56140), 282 (65610). ESI Mass Spectrum (m/z) (positive mode): 298.9 ($[M]^{4+}/4$), 446.6 ($[M+PF_6]^{3+}/3$), 742.3 ($[M+2PF_6]^{2+}/2$). Anal. Found: C, 49.96; H, 3.59; N, 7.73; Ru, 5.55; P, 7.12; F, 26.41. Calcd for $C_{74}H_{64}N_{10}RuP_4F_{24}$ (%): C, 50.09; H, 3.64; N, 7.89; Ru, 5.70; P, 6.98; F, 25.70.

$[Zn(L_1)_2] \cdot (PF_6)_4$ - (Zn-1). **Zn-1** was synthesized and purified following the procedure described for **Ru-1**, starting from $[Zn(L_1)Cl_3]$ (0.072 g, 0.1 mmol) and $L_1 \cdot Br$ (0.063 g, 0.1 mmol). (Yield, 141 mg, 81%).

^{1}H NMR (DMSO-d_6), δ ppm: 9.37 (s, 4H), 9.10 (d, 4H, ^3J = 7.7 Hz), 8.98 (d, 4H, ^3J = 6.2 Hz), 8.47 (d, 4H, ^3J = 7.7 Hz), 8.28 (d, 4H, ^3J = 6.9 Hz), 8.14 (d, 4H, ^3J = 6.9 Hz), 8.00 (d, 2H, ^3J = 15.4 Hz), 7.94−7.88 (m, 8H), 7.62 (d, 4H, ^3J = 9.2 Hz), 7.49 (d, 4H, ^3J = 6.9 Hz), 7.22 (d, 2H, ^3J = 15.4 Hz), 6.80 (d, 4H, ^3J = 9.2 Hz), 5.83 (s, 4H, $-CH_2$-py$^+$), 3.03 (s, 12H, N$-CH_3$). UV−visible (CH_3CN) [λ_{max} (nm); (ε_{max}) (M^{-1} cm^{-1})]: 487 (83130), 285 (80080). ESI Mass Spectrum (m/z) (positive mode): 289.4 ($[M]^{4+}/4$), 434 ($[M+PF_6]^{3+}/3$), 724.3 ($[M+2PF_6]^{2+}/2$). Anal. Found: C, 51.03; H, 3.62; N, 7.99; Zn, 3.58; P, 7.24; F, 26.36. Calcd for $C_{74}H_{64}N_{10}ZnP_4F_{24}$ (%): C, 51.12; H, 3.71; N, 8.06; Zn, 3.76; P, 7.13; F, 26.23.

$[Ru(tpy\text{-}NMe_2)(L_1)] \cdot (PF_6)_3$ - (Ru-1′). $[Ru(L_1)Cl_3] \cdot Cl$ (0.079 g, 0.1 mmol) and tpy-NMe_2 (0.036 g, 0.1 mmol) were refluxed for one night in a mixture of EtOH/H_2O/DMF (45/15/3 mL). After cooling, an aqueous solution of NH_4PF_6 (200 mg, 5 mL) was added. The resulting mixture was concentrated under vacuum to about 25 and 80 mL of water were added. The dark-red solid obtained was filtered, washed successively with water (3 × 10 mL), ethanol (3 × 10 mL) and diethyl ether (3 × 10 mL). Slow diffusion of ether onto a solution of **Ru-1′** in acetonitrile produced a precipitate, which was collected by filtration (Yield, 0.102 g, 71%).

^{1}H NMR (DMSO-d_6), δ ppm: 9.45 (s, 2H), 9.36 (s, 2H), 9.10 (d, 4H, ^3J = 8.7 Hz), 9.08 (d, 2H, ^3J = 6.5 Hz), 8.81 (m, 2H), 8.49 (d, 2H, ^3J = 8.1 Hz), 8.36 (d, 2H, ^3J = 8.3 Hz), 8.21−8.00 (m, 6H), 7.90 (d, 2H, ^3J = 6.5 Hz), 7.60 (dd, 2H, ^3J = 8.3 Hz), 7.58 (d, 2H, ^3J = 8.3 Hz), 7.53 (d, 2H, ^3J = 8.3 Hz), 7.30−7.20 (m, 4H), 7.01 (d, 2H, ^3J = 8.9 Hz), 6.91 (d, 1H, ^3J = 8.7 Hz), 6.80 (d, 1H, ^3J = 8.7 Hz), 5.84 (s, 2H, $-CH_2$-py$^+$), 3.13 (s, 6H, N$-CH_3$), 3.03 (s, 6H, N$-CH_3$). UV−visible (CH_3CN) [λ_{max} (nm); (ε_{max}) (M^{-1} cm^{-1})]: 500 (45020), 308 (57750), 283 (51240). ESI Mass Spectrum (m/z) (positive mode): 333.6 ($[M]^{3+}/3$), 572.9 ($[M+PF_6]^{2+}/2$). Anal. Found: C, 50.28; H, 3.73; N, 8.91; Ru, 7.12; P, 6.64; F, 23.97. Calcd for $C_{60}H_{52}N_9RuP_3F_{18}$ (%): C, 50.22; H, 3.65; N, 8.78; Ru, 7.04; P, 6.48; F, 23.83.

$[Zn(tpy\text{-}NMe_2)(L_1)] \cdot (PF_6)_3$ - (Zn-1′). $[Zn(L_1)Cl_3]$ (0.072 g, 0.1 mmol) and tpy-NMe_2 (0.036 g, 0.1 mmol) were refluxed for one night in a mixture of EtOH/H_2O (50/20 mL). The resulting solution was cooled to room temperature and concentrated under reduced pressure to about 25 mL. Then, water (80 mL) was added, followed by an aqueous solution of NH_4PF_6 (200 mg, 5 mL). The resulting orange-red solid was filtered, washed successively with ethanol (3 × 10 mL) and diethyl ether (3 × 10 mL). As for **Ru-1′**, the product was purified by addition of diethyl ether to a solution of **Zn-1′** in acetonitrile (Yield, 110 mg, 78%).

^{1}H NMR (DMSO-d_6), δ ppm: 9.36 (s, 2H), 9.25 (s, 2H), 9.13 (d, 2H, ^3J = 10 Hz), 9.11 (d, ^3J = 10 Hz, 2H), 9.00 (d, 2H, ^{3}

J = 6.2 Hz), 8.48 (d, 2H, ^3J = 6.9 Hz), 8.40 (d, 2H, ^3J = 8.5 Hz), 8.27 (d, 4H, ^3J = 6.9 Hz), 8.15 (d, 2H, ^3J = 5.4 Hz), 8.01 (d, 1H, ^3J = 15.4 Hz), 8.00−7.88 (m, 6H), 7.62 (d, 2H, ^3J = 7.7 Hz), 7.48 (m, 4H), 7.22 (d, 1H, ^3J = 15.4 Hz), 6.99 (d, 2H, ^3J = 7.7 Hz), 6.80 (d, 2H, ^3J = 8.5 Hz), 5.84 (s, 2H, $-CH_2$-py$^+$), 3.13 (s, 6H, N$-CH_3$), 3.04 (s, 6H, N$-CH_3$). UV−visible (CH_3CN) [λ_{max} (nm); (ε_{max}) (M^{-1} cm^{-1})]: 481 (41020), 445 (40040), 325 (34330), 313 (35140), 285 (64310), 236 (46860). ESI Mass Spectrum (m/z) (positive mode): 321.2 ($[M]^{3+}/3$), 553.9 ($[M+PF_6]^{2+}/2$). Anal. Found: C, 51.42; H, 3.70; N, 8.94; Zn, 4.58; P, 6.72; F, 24.56. Calcd for $C_{60}H_{52}N_9ZnP_3F_{18}$ (%): C, 51.50; H, 3.75; N, 9.01; Zn, 4.67; P, 6.64; F, 24.44.

[Ru(L$_2$)$_2$]·(PF$_6$)$_6$ - (Ru-2). Ru-2 was prepared according to the procedure described for **Ru-1**, starting from [Ru(**L$_2$**)Cl$_3$]·Cl$_2$ (0.106 g, 0.1 mmol) and **L$_2$**·Cl$_2$ (0.085 g, 0.1 mmol). The purification process was identical to that used for **Ru-1** (R_f = 0.3, Al_2O_3). (Yield, 0.129 g, 51%).

^{1}H NMR (DMSO-d_6), δ ppm: 9.40 (s, 4H), 8.91 (d, 8H, ^3J = 6.2 Hz), 8.55 (d, 4H, ^3J = 2 Hz), 8.15 (d, 8H, ^3J = 6.2 Hz), 8.10 (m, 8H), 7.98 (d, 4H, ^3J = 16.2 Hz), 7.71 (t, 2H, ^3J = 2 Hz), 7.60 (d, 8H, ^3J = 8.5 Hz), 7.53 (d, 4H, ^3J = 5.4 Hz), 7.34 (d, 4H, ^3J = 5.4 Hz), 7.22 (d, 4H, ^3J = 16.2 Hz), 6.79 (d, 8H, ^3J = 8.5 Hz), 5.86 (s, 8H, $-CH_2$-py$^+$), 3.03 (s, 24H, N$-CH_3$). UV−visible (CH_3CN) [λ_{max} (nm); (ε_{max}) (M^{-1} cm^{-1})]: 494 (141350), 310 (80960), 282 (64190). ESI Mass Spectrum (m/z) (positive mode): 278.3 ($[M]^{6+}/6$), 363.2 ($[M+PF_6]^{5+}/5$), 490 ($[M+2PF_6]^{4+}/4$), 701.4 ($[M+3PF_6]^{3+}/3$), 1124.8 ($[M+4PF_6]^{2+}/2$). Anal. Found: C, 49.98; H, 3.82; N, 7.65; Ru, 3.83; P, 7.41; F, 27.16. Calcd for $C_{106}H_{98}N_{14}RuP_6F_{36}$ (%): C, 50.15; H, 3.89; N, 7.72; Ru, 3.98; P, 7.32; F, 26.94.

[Ru(bpy)$_2$(L$_3$)]·(PF$_6$)$_4$ - (Ru-3). [Ru(bpy)$_2$Cl$_2$] (0.048 g, 0.1 mmol) and **L$_3$**·(PF$_6$)$_2$ (0.092 g, 0.1 mmol) were suspended in aqueous-acetonitrile mixed medium (15/55 mL). The reaction mixture was stirred overnight at reflux. After cooling, the red solution was concentrated under reduced pressure to about 25 mL, and the crude product was precipitated using a concentrated aqueous solution of ammonium hexafluorophosphate. The crude product was purified by column chromatography (Al_2O_3, sat. aq.KNO_3/CH_3CN: 20/180 (to elute the impurity), followed by sat. aq. $NaPF_6$/CH_3CN: 20/180 (to elute the expected complex). **Ru-2** was precipitated after concentration of the second eluted fraction under reduced pressure and addition of a concentrated aqueous solution of NH_4PF_6. The precipitate was washed with ethanol (2 × 10 mL) and dried with diethyl ether (2 × 10 mL). (Yield, 0.078 g, 78%).

^{1}H NMR (DMSO-d_6), δ ppm: 8.87 (d, 2H, ^3J = 8.5 Hz), 8.78 (d, 2H, ^3J = 8.3 Hz), 8.73 (d, 2H, ^3J = 8.1 Hz), 8.57 (d, 4H, ^3J = 6.7 Hz), 8.17−7.97 (m, 12H), 7.76 (d, 2H, ^3J = 5.2 Hz), 7.64 (d, 4H, ^3J = 8.9 Hz), 7.60 (d, 2H, ^3J = 5.2 Hz), 7.46 (m, 6H), 7.22 (d, 2H, ^3J = 16 Hz), 6.82 (d, 4H, ^3J = 8.9 Hz), 5.60 (s, 4H, $-CH_2$-py$^+$), 3.03 (s, 12H, N$-CH_3$). UV−visible (CH_3CN) [λ_{max} (nm); (ε_{max}) (M^{-1} cm^{-1})]: 495 (104620), 286 (98330). ESI Mass Spectrum (m/z) (positive mode): 261 ($[M]^{4+}/4$), 396.6 ($[M+PF_6]^{3+}/3$), 667.3 ($[M+2PF_6]^{4+}/2$). Anal. Found: C, 45.76; H, 3.56; N, 8.56; Ru, 6.13; P, 7.75; F, 28.22. Calcd for $C_{62}H_{58}N_{10}RuP_4F_{24}$ (%): C, 45.85; H, 3.60; N, 8.62; Ru, 6.22; P, 7.63; F, 28.07.

Results and Discussion

Synthesis of the Pro-Ligands and Complexes. All pro-ligands **L$_1$**, **L$_2$**, and **L$_3$** were prepared according to a similar strategy. Reaction at reflux for one night in acetonitrile of brominated terpyridine (4′-(4-bromomethylphenyl)-2,2′,6′,2″-terpyridine {tpy-CH_2Br}, 4′-(3,5-di(bromomethyl)-phenyl)-2,2′,6′,2″-terpyridine {tpy-(CH_2Br)$_2$}) or brominated bipyridine (5,5′-di(bromomethyl)-2,2′-bipyridine {bpy-(CH_2Br)$_2$}), with 4-(4-*N,N*-dimethylaminostyryl)-pyridine (*DASpyr*) afforded salts {4′-{4-(4-*N,N*-dimethylaminostyryl-4-pyridiniumyl) methyl}-2,2′:6′,2″-terpyridine bromide} (**L$_1$**·Br), {4′-(3,5-bis{[4-*N,N*-dimethylaminostyryl-4-pyridiniumyl]methyl})-2,2′:6′,2″-terpyridine hexafluorophosphate} (**L$_2$**·(PF$_6$)$_2$), and {5,5′-di([4-*N,N*-dimethylaminostyryl-4-pyridiniumyl] methyl)-2,2′bipyridine hexafluorophosphate} (**L$_3$**·(PF$_6$)$_2$), respectively, with yields ranging from 79% to 93% after purification.

The strategy generally employed to purify charged metal complexes from free pro-ligands using selective precipitation by counterion exchange, for example, from halide anions to hexafluorophosphate anions, was not adapted for the purification of the metal complexes synthesized in this article. Since pro-ligands **L$_1$**, **L$_2$**, and **L$_3$** are positively charged they co-precipitated with the metal complexes during the counterion exchange process. Accordingly, complexes **M-1**, **M-1′** (with M = Ru, Zn), and **Ru-2** were prepared in two steps. [(**L$_1$**)RuCl$_3$]Cl, [(**L$_1$**)ZnCl$_3$], and [(**L$_2$**)RuCl$_3$]Cl$_2$ were first isolated and were then reacted either with 1 equiv of the neutral ligand (tpy-NMe$_2$) or with 1 equiv of the appropriate cationic ligand. Purification of the final metal complexes was finally realized either by selective precipitation for **M-1′** or by chromatography on neutral alumina for **M-1** and **Ru-2**. Finally, [Ru(bpy)$_2$(**L$_3$**)]$^{4+}$ (**Ru-3**) was obtained by reaction of equimolar amounts of Ru(bpy)$_2$Cl$_2$ and **L$_3$**·(PF$_6$)$_2$ and purified by column chromatography.

All pro-ligands and metal complexes studied in this article were fully characterized by elemental analysis, multidimensional NMR spectroscopic methods, mass spectrometry, and absorption spectroscopy (see Experimental Section). All the ^{1}H and ^{13}C NMR spectra were recorded in DMSO-d_6 and characteristic features were obtained in all these spectra. For instance in the ^{1}H NMR spectra, *N*-alkylation of the 4′-pyridyl pendant group from the $DASP^+$ moiety with the different bromo-derivatives was evidenced by the presence of a single peak at δ = 5.8−5.9 ppm assigned to the pyridinium-CH_2 group. An exception was observed for **Ru-3** for which this signal was shielded to 5.6 ppm instead of 5.81 ppm for free **L$_3$**. This unexpected shift is certainly due to the close proximity to the metal center of this methylene group. In addition to the signal corresponding to the pyridinium-CH_2 group, the presence of the $DASP^+$ moiety was also supported by the presence of a characteristic set of six doublets, two of them attributed to the two vinylic protons in *trans* configuration showing a strong coupling of ∼16 Hz. ^{1}H NMR spectra of **L$_3$** and **Ru-3** are shown in Figure S4 (Supporting Information) to illustrate the influence of the metallic center on the characteristic peaks of **L$_3$**.

Pro-ligands and metal complexes were also characterized using mass spectrometry. A single quadrupole mass spectrometer and a triple quadrupole mass spectrometer have been used to characterize the ligands and metal complexes. A systematic fragmentation of the complexes at the pyridinium group was observed with the single quadrupole mass spectrometer and only few ligands were characterized with this apparatus. Typical examples of mass spectra are shown in Figure S5 (Supporting Information). In the case of **L$_2$**, one single peak was observed at m/z = 391.9 and was attributed to $[\mathbf{L_2}]^{2+}/2$. The five peaks observed in the mass spectrum

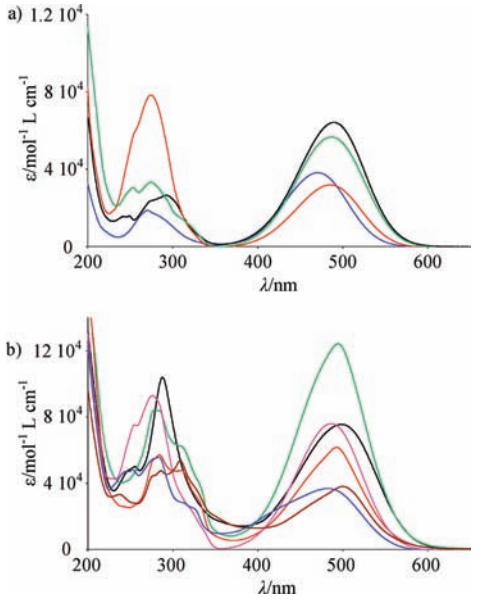

Figure 1. Absorption spectra of (a) Me-*DASP*$^+$ (blue line), $\mathbf{L_1}$ (red line), $\mathbf{L_2}$ (green line), and $\mathbf{L_3}$ (black line) and (b) metal complexes **Ru-1** (red line), **Ru-1′** (brown line), **Ru-2** (green line), **Ru-3** (black line), **Zn-1** (pink line), and **Zn-1′** (blue line), at 298 K in acetonitrile.

of **Ru-2** were attributed to the five different states of charge (z) corresponding to the ion pairs of general formula $[Ru(\mathbf{L_2})_2 + x\ PF_6]^{z+}$, with $z = 6 - x$ and $0 \leq x \leq 4$. For all these peaks, the envelope of the isotopic pattern was in good agreement with the simulated ones.

UV/vis spectroscopy. Absorption spectra were recorded in acetonitrile at room temperature using the hexafluorophosphate salt of all pro-ligands and metal complexes. Spectra of the three pro-ligands and the six metal complexes, together with the reference spectrum of Me-*DASP*·(PF_6), are shown in Figure 1. The most relevant spectroscopic results are summarized in Table 1.

The electronic absorption spectra of $\mathbf{L_1}$, $\mathbf{L_2}$, and $\mathbf{L_3}$ (Figure 1a) show a broad and intense band in the visible region, corresponding to $\pi(-NMe_2) \rightarrow \pi^*$(pyridinium) intramolecular charge transfer (ICT) excitations from the $-NMe_2$ electron donor groups to the pyridinium acceptors. The absorption maximum of the three pro-ligands is centered at 485 nm, which is slightly shifted compared to the free Me-*DASP*$^+$ (469 nm). This bathochromic shift is in accordance with results previously reported in the literature with *DASP*$^+$ derivatives bearing aromatic groups.[52,53] The intensity of the ICT band depends on the number of *DASP*$^+$ groups linked to the pro-ligands. Consequently, the molar absorptivity of $\mathbf{L_2}$ bearing two *DASP*$^+$ ($\varepsilon \sim 65 \times 10^3\ M^{-1}.cm^{-1}$) is 2-fold higher compared to $\mathbf{L_1}$ containing only one chromophore ($\varepsilon \sim 33 \times 10^3\ M^{-1}.cm^{-1}$). At higher energies, feature bands are ascribed to $\pi \rightarrow \pi^*$ transitions.

As expected for such polypyridinic metal complexes, all the ruthenium and zinc complexes show intense bands in the UV region of the spectrum (250−320 nm).

Table 1. Electronic Absorption Data and Assignments[a]

compound	λ_{max} [nm]	E_{max} [ICT] [eV]	ε [M^{-1} cm^{-1}][b]	assignment
Me-*DASP*$^+$	469	2.64	38100	ICT[c]
	270	4.59	17800	$\pi \rightarrow \pi^*$
$\mathbf{L_1}$	485	2.56	33400	ICT[c]
	272	4.56	77700	$\pi \rightarrow \pi^*$
$\mathbf{L_2}$	485	2.56	65400	ICT[c]
	274	4.53	35400	$\pi \rightarrow \pi^*$
$\mathbf{L_3}$	486	2.55	78100	ICT[c]
	287	4.32	29500	$\pi \rightarrow \pi^*$
Ru-1	493	2.52	71800	d $\rightarrow \pi^*$ and ICT
	310	4.00	56100	$\pi \rightarrow \pi^*$
	282	4.40	65600	$\pi \rightarrow \pi^*$
Ru-2	494	2.51	141300	d $\rightarrow \pi^*$ and ICT
	310	4.00	69000	$\pi \rightarrow \pi^*$
	282	4.40	92000	$\pi \rightarrow \pi^*$
Ru-3	495	2.51	83000	d $\rightarrow \pi^*$and ICT
	286	4.34	113000	$\pi \rightarrow \pi^*$
Ru-1′	500	2.48	45000	d $\rightarrow \pi^*$ and ICT
	308	4.03	57700	$\pi \rightarrow \pi^*$
	283	4.38	51200	$\pi \rightarrow \pi^*$
Zn-1	487	2.55	83100	ICT[c]
	285	4.35	80100	$\pi \rightarrow \pi^*$
Zn-1′	481	2.58	41000	ICT[c]
	445	2.79	40000	ICT[d]
	325	3.82	34300	$\pi \rightarrow \pi^*$
	313	3.96	35100	$\pi \rightarrow \pi^*$
	285	4.35	64300	$\pi \rightarrow \pi^*$
	236	5.25	46900	$\pi \rightarrow \pi^*$

[a] In acetonitrile, at 298 K. [b] Calculated using 2.5×10^{-5}, 10^{-5}, 5×10^{-6}, and 2.5×10^{-6} mol L^{-1} solutions. [c] Intramolecular charge transfer $\pi(-C_6H_4\text{-}4\text{-}NMe_2) \rightarrow \pi^*(pyr^+)$. [d] Intramolecular charge transfer $\pi(-C_6H_4\text{-}4\text{-}NMe_2) \rightarrow \pi^*$(terpyridine).

These bands can be attributed to $\pi \rightarrow \pi^*$ transitions from the aromatic groups. In the 400−600 nm region, ruthenium complexes **Ru-1**, **Ru-2**, and **Ru-3** exhibit a broad and intense absorption band due to intraligand charge transfer excitations of the *DASP*$^+$ moiety, which overlaps the less intense $d(Ru^{II}) \rightarrow \pi^*(L)$ MLCT bands (Figure 1b and see below). In the specific case of **Ru-1′**, which contains two push−pull systems, the band centered at 500 nm is the result of the contribution of the ICT band of the *DASP*$^+$, the ICT band of tpy-NMe_2 complexing Ru^{II}, and the $d(Ru^{II}) \rightarrow \pi^*(L)$ MLCT band.

Contributions to the visible band are different for complexes **Zn-1** and **Zn-1′**. Because of the very high third ionization potential of zinc(II) cation, zinc(II) cation does not engage in MLCT transitions, at least at low wavelength in the UV−visible region. This was confirmed by DFT calculations performed on metal complexes which proved for d^{10} metal complexes of 1*H*-[1,10]-phenanthrolin-2-one that the highest occupied molecular orbitals (HOMOs) were essentially ligand-based.[54] As a consequence, the band observed for **Zn-1** at 487 nm can be mainly assigned to the ICT excitation of the *DASP*$^+$ moiety. Concerning the intensity of this band, complex **Zn-1** contains two *DASP*$^+$ and accordingly a 2-fold increase of the intensity of the band is observed compared with $\mathbf{L_1}$. For **Zn-1′**, the band centered at 481 nm is also assigned to the ICT excitations of the *DASP*$^+$ moiety but a noticeable contribution, attributed to the ICT of the tpy-NMe_2 ligand,[22] was evidenced by a shoulder at about 445 nm.

(52) Coe, B. J.; Harris, J. A.; Asselberghs, I.; Clays, K.; Olbrechts, G.; Persoons, A.; Hupp, J. T.; Johnson, R. C.; Coles, S. J.; Hurthouse, M. B.; Nakatani, K. *Adv. Funct. Mater.* **2002**, *12*, 110–116.
(53) Clays, K.; Coe, B. J. *Chem. Mater.* **2003**, *15*, 642–648.
(54) Zheng, S.-L.; Zhang, J.-P.; Chen, X.-M.; Huang, Z.-L.; Lin, Z.-Y.; Wong, W.-T. *Chem.—Eur. J.* **2003**, *9*, 3888–3896.

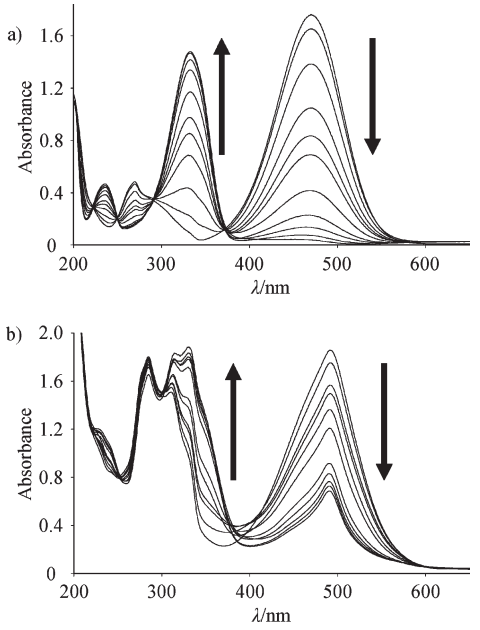

Figure 2. Evolution of the absorption spectra in acetonitrile at 298 K of Me-*DASP*$^+$ (top) and **Ru-1** (bottom) with addition of increasing amounts of HCl.

For Ru^{II} complexes, the contribution of the ICT transition can be removed by protonation of the $DASP^+$ moiety to confirm the role of the MLCT bands in the visible region of the absorption spectra. As shown in Figure 2a for Me-$DASP^+$, the dimethylamino group of the push−pull fragment loses its donating ability when protonated. Protonation of the different ruthenium complexes led to the progressive disappearance of the ICT transition band and therefore the progressive increase of the contribution of the classical MLCT band of the $\{Ru(tpy)_2\}^{2+}$ fragment to the absorption in the visible region, as illustrated for **Ru-1** in Figure 2b.[55] This study thus confirmed that the absorption band observed in the visible region of the ruthenium complexes correspond to the superposition of both the ICT band of the push−pull $DASP^+$ and the $d(Ru^{II}) \rightarrow \pi^*(L)$ MLCT band. Isosbestic points are clearly noticed in Figure 2a, indicating a nice clean change with protonation of Me-$DASP^+$. On the other hand, the absence of isosbestic points in Figure 2b suggests the generation of multiple species. Protonation of **Ru-1** required the use of a strong acid and was kinetically slow, resulting in the formation of three different species, namely, non-, mono-, and diprotonated complexes.

The results of the analysis of the absorption properties of the metal complexes clearly show that the push−pull $DASP^+$ fragment retains its own chromophoric properties when covalently connected to the polypyridyl metal complexes. This absence of reciprocal influence between the organic dye and the polypyridyl metal fragment is certainly due to the type of linkage used to connect both components in this study, namely a nonconjugated spacer which isolates the dye from the metal complex.

Luminescence Spectroscopy. Luminescence data were measured in acetonitrile at 298 K. One of the aims of this work was to synthesize and characterize a series of terpyridinic complexes exhibiting a detectable emission state at room temperature to further use these systems, for example, to generate multifunctional nanocomposites.[30] $[Ru(bpy)_2(dmb)]^{2+}$ (dmb = 4,4′-dimethylbipyridine)[56] was used as the reference to estimate the luminescence quantum yields of the compounds. The photoluminescence spectra have been recorded upon excitation at 469 nm, corresponding to the maximum absorption wavelength of the ICT of Me-$DASP^+$. Emission spectra of the ligands and metal complexes are shown in Figure 3 and Figure 4. Luminescence data are given in Table 2.

The fluorescence properties of the three ligands $\mathbf{L_1}$, $\mathbf{L_2}$, and $\mathbf{L_3}$ and the reference free Me-$DASP^+$ are comparable (Figure 3). The maximum emission wavelength of the three ligands is comprised between 619 and 625 nm, which is slightly higher than the maximum emission wavelength observed for Me-$DASP^+$ (613 nm). A similar trend was observed in the absorption spectra. Moreover, the

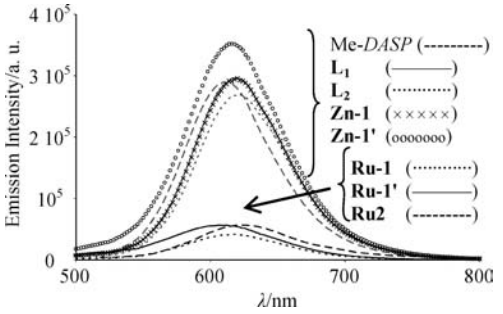

Figure 3. Emission spectra of Me-$DASP^+$, $\mathbf{L_1}$, $\mathbf{L_2}$, $\mathbf{L_3}$, **M-1**, **M-1′** (M = Ru, Zn), and **Ru-2** in acetonitrile at 298 K.

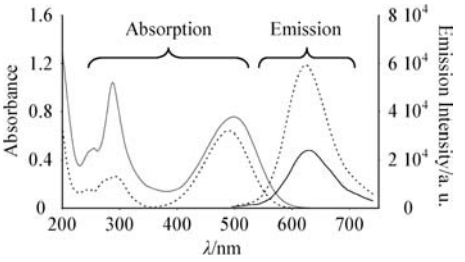

Figure 4. Absorption and emission spectra of $\mathbf{L_3}$ (dotted lines) and **Ru-3** (full lines), at 298 K in acetonitrile.

Table 2. Luminescence Data at 298 K[a]

compound	λ_{max} [nm]	Φ_r ($\times 10^{-2}$)	η_1[b]	η_2[c]
$\{Ru(bpy)_2(dmb)\}^{2+}$	613	6.2[d]	100	475
Me-DASP$^+$	613	1.3	21	100
$\mathbf{L_1}$	619	1.43	23	110
$\mathbf{L_2}$	623	1.31	21	100
$\mathbf{L_3}$	625	1	16	77
Ru-1′	612	0.31	5	24
Ru-1	617	0.22	4	17
Ru-2	626	0.29	4	22
Ru-3	630	0.26	4	20
Zn-1′	618	1.66	26	127
Zn-1	620	1.45	23	111

[a] In acetonitrile, upon excitation at 469 nm. [b] $\eta_1 = (\Phi_{Ru(bpy)2(dmb)}/\Phi_r) \times 100$. [c] $\eta_2 = (\Phi_{Me\text{-}DASP+}/\Phi_r) \times 100$. [d] Ref 50.

(55) Beley, M.; Collin, J.-P.; Sauvage, J.-P.; Sugihara, H.; Heisel, F.; Miehé, A. *J. Chem. Soc., Dalton Trans.* **1991**, 3157–3159.

(56) Ross, H. B.; Boldaji, M.; Rillema, D. P.; Blanton, C. B.; White, R. P. *Inorg. Chem.* **1989**, *28*, 1013–1021.

luminescence quantum yields of L_1, L_2, and L_3 are not much altered by the presence of the polypyridinic fragment.

The maximum emission wavelength of the metal complexes is comparable to that of the free ligands from which they were synthesized. This suggests that the fluorescence of the metal complexes is mainly due to the contribution of the fluorescence from the push−pull $DASP^+$. In addition, terpyridinic Ru^{II} and Zn^{II} complexes are known to exhibit no efficient luminescence at room temperature. In the case of **Zn-1** and **Zn-1′**, the maximum emission wavelength and the luminescence quantum yield are similar to those of ligand L_1. This shows that there is no influence of the metal center on the fluorescence properties of the zinc complexes. In the case of **Ru-1**, **Ru-1′**, and **Ru-2**, no matter how many $DASP^+$ groups are covalently connected to the polypyridyl ruthenium fragment, the luminescence quantum yield of the ruthenium complex is significantly reduced by about 75% compared with the luminescence quantum yield of the corresponding free ligand. The quenching of fluorescence might rely on an intramolecular photoinduced electron transfer from the excited Ru^{II} polypyridyl complex (donor) to the $DASP^+$ group (acceptor). Nevertheless, it has to be highlighted that despite the quenching observed, the fluorescence of all the terpyridyl ruthenium complexes remains detectable at room temperature. For **Ru-3**, both individual components of the complexes, namely, the $\{(bpy)Ru(dmb)\}^{2+}$ fragment and the $DASP^+$ groups, display an emission band centered at 613 nm with luminescence quantum yields of 6.2 and 1.3, respectively (Table 2). However, the luminescence quantum yield for **Ru-3** is only 0.26. An intramolecular photoinduced electron transfer from the excited Ru^{II} polypyridyl fragment to the $DASP^+$ group is likely responsible for the luminescence quantum yield reduction of both entities, but energy transfer between the $DASP^+$ group and the polypyridyl ruthenium fragment can not be excluded.

Electrochemistry. Figure 5 shows the oxidation behavior of complexes **Ru-1′**, **Zn-1**, and **Zn-1′**. The comparison between **Zn-1′** and **Zn-1** (Figure 5) enables us to ascribe the two successive waves respectively to the oxidation of the dimethylaniline moiety on the $DASP^+$ arm for the first one and the other dimethylaniline for the second one. Surprisingly the signal at higher potential is reversible while the one at lower potential is not. This is probably due to the inability of the pyridinium moiety to efficiently stabilize the cation radical form of the dimethylaniline moiety. Note that the relative intensities for the $DASP^+$ oxidation in **Zn-1** and **Zn-1′** correlates with the actual number of *DASP* units in each complex. The irreversible chemical reaction involving the coupling of the cation radical of the $DASP^+$ ligand shifts the oxidation potential of the dimethylaniline to lower values, hence explaining the relative order of the two signals in **Zn-1′** and **Ru-1′**. The CV for **Ru-1′** exhibits the additional response of the metal center compared to the similar **Zn-1′**. The oxidation potential for $Ru^{II} \rightarrow Ru^{III}$ is very close to the similar one in $[Ru(tpy)_2]^{2+}$. The relative order of the two oxidation waves agrees with the order of the corresponding orbitals (see below) with the HOMO centered on the ligand and lower energy occupied MOs centered on the metal.

Figure 6 shows the cathodic behavior of **Ru-1** and **Ru-1′**, with the successive reductions of the pyridinium

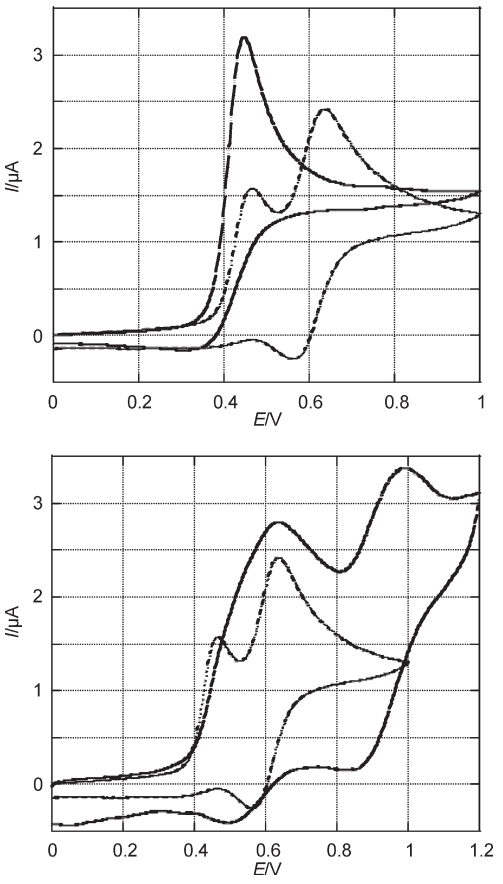

Figure 5. Cyclic voltammograms of **Zn-1** (full line) and **Zn-1′** (dashed line) in acetonitrile + $TBAPF_6$ on Pt (top) and CVs of **Zn-1′** (dashed line) and **Ru-1′** (full line) in acetonitrile + $TBAPF_6$ on Pt (bottom).

moiety in $DASP^+$ (first wave) and terpy ligands (second and third waves). As expected the reduction potential for the pyridinium in $DASP^+$ is much more negative than when pyridinium is only linked to terpy.[33] The reduction of the tpy ligands in the complexes appears at potentials very close to the one of tpy, and slightly more negative in **Ru-1′** than in **Ru-1** (see Table 3).

Hence, it seems that the dimethylaniline moiety has very little influence on the reduction potentials of the tpy ligands. Figure 6 shows the comparison between CVs of **Ru-2** and **Ru-3**, with the first irreversible reduction of pyridinium and following reversible reductions of tpy or bpy ligands. As expected, the current ratio between tpy and pyridinium in **Ru-2** on one hand and bpy and pyridinium in **Ru-3** on the other hand agrees well with the respective complex formulas. As already mentioned for the parent $Ru(tpy)_2^{2+}$ and $Ru(bpy)_3^{2+}$ complexes, bpy reductions occur at potentials slightly more cathodic than tpy ones.[57]

Finally, Table 3 summarizes the redox potential data for the ligands and corresponding complexes. In the free ligands, only the irreversible pyridinium reduction is seen in the potential window explored, while dimethylaniline oxidation involves generally a two-step process featured by the two successive waves.

Theoretical Calculations. Density functional theory (DFT) and time-dependent (TD) DFT calculations were

(57) Constable, E. W.; Figgemeier, E.; Housecroft, C. H.; Olsson, J.; Zimmermann, Y. C. *Dalton Trans.* **2004**, 1918.

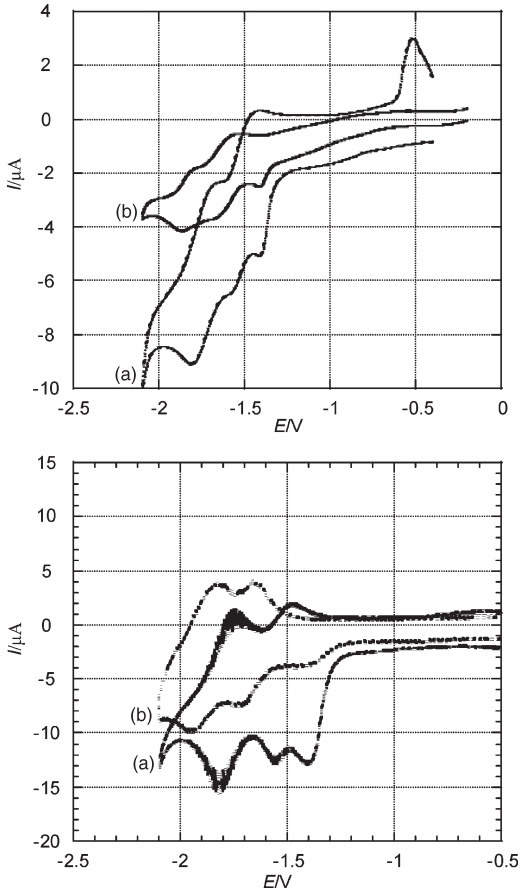

Figure 6. Cyclic Voltammograms of **Ru-1** (a) and **Ru-1′** (b) in acetonitrile + $TBAPF_6$ on Pt (top) and CVs of **Ru-2** (a) and **Ru-3** (b) in acetonitrile + $TBAPF_6$ on Pt (bottom).

Table 3. Electrochemical Data Deduced from CV Experiments

compound	oxidation potentials (V vs Ag^+/Ag)	reduction potentials (V vs Ag^+/Ag)
Ru-1′	0.63[a]; 0.92(134)	−1.41; −1.61 (130); −1.84 (70)
Ru-1	0.50[a]; 0.70(105); 0.90(54)	−1.39[a]; −1.53(160); −1.73 (140)
Zn-1′	0.49[a]; 0.60(78)	−1.41 ; −1.62(140); −1.74 (170)
Zn-1	0.45[a]	−1.40 ; −1.52 (90); −1.69 (80)
Ru-2	0.53[a]; 1.00(66)	−1.40[a]; −1.51 (80); −1.79 (65)
Ru-3	0.54[a]; 1.00(62)	−1.42[a]; −1.68(64); −1.89(130)
$\mathbf{L_1}$	0.47[a]; 0.87[a]	−1.40[a]
$\mathbf{L_2}$	0.44[a]; 0.88[a]	−1.35[a]
$\mathbf{L_3}$	0.51[a]	−1.33[a]

[a] Irreversible system. All potentials are measured in acetonitrile + $TBAPF_6$ 0.1 M dried over molecular sieves. In brackets the peak-to-peak separation.

performed to investigate the structural, electronic and optical properties of ligands $\mathbf{L_1}$, $\mathbf{L_2}$, and $\mathbf{L_3}$ and the ruthenium based complexes. All calculations were performed using the Gaussian03 program. No symmetry constraints were imposed on any geometry optimizations, and the Cartesian coordinates of the resulting optimized geometries are provided as Supporting Information. The charged ligands were optimized first using the B3LYP functional[58,59] together with the 6-31G-(d) basis set[60] not including counteranions.

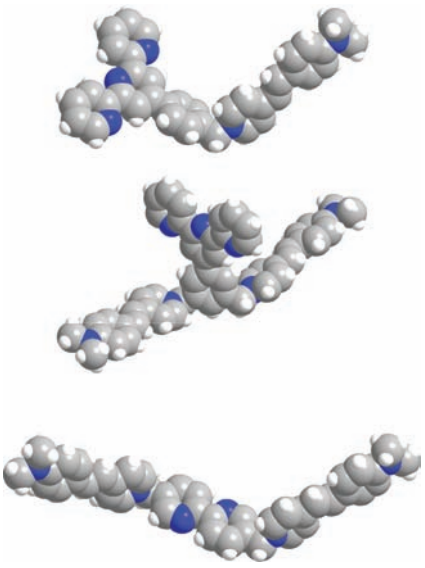

Figure 7. Calculated structure of ligands $\mathbf{L_1}$ (top), $\mathbf{L_2}$ (middle), and $\mathbf{L_3}$ (bottom). Carbon, gray; hydrogen, white; nitrogen, blue.

In the calculated structure (Figure 7) for $\mathbf{L_1}$ and $\mathbf{L_2}$ the terpyridine moieties were found to be almost coplanar with adjacent pyridine rings being antiparallel (N−C−C−N dihedral angles varies between 178.1 and 179.8° and the calculated angles between the mean planes range from 0.2 to 2.1°). The phenyl ring and the central pyridine of the terpyridine are twisted by 35° because of steric interactions between hydrogen atoms. The presence of a methylene residue between the phenyl and the $DASP^+$ leads to a highly distorted structure. For $\mathbf{L_1}$, the $DASP^+$ and phenyl planes were found to have an angle of 88°, and $DASP^+$ and terpyridine planes (considering the central pyridine) make a 64.5° angle. For $\mathbf{L_2}$, these angles were found to be 86 and 89.9° between phenyl and $DASP^+$ and 77.6 and 81.6° between terpyridine and $DASP^+$. Furthermore, the two $DASP^+$ moieties point in opposite directions from the phenyl ring. Ligand $\mathbf{L_3}$, despite its different nature, presents similar features: nearly coplanar and antiparallel pyridine rings (N−C−C−N dihedral angle 178.6 and 1.7° between their mean planes) and $DASP^+$ moieties pointing in opposite directions from the bipyridine at 80.8 and 85° angles.

The electronic structure and excited states of the ligands were then calculated at a higher level of theory using PBE0[61] hybrid exchange correlation functional, casting 25% of exact HF exchange into the PBE exchange and correlation functional. This hybrid functional has been chosen because it generally outperforms other global hybrids in the computation of UV−vis spectra and was found to give reliable results in the prediction of molecular properties of both large organic molecules[62] and complex systems containing Ru atom.[63] In terms of basis sets, the triple-ζ split valence basis 6-311+G(d,p) was used. Surprisingly, for $\mathbf{L_1}$ the two highest occupied orbitals (HOMO and HOMO-1) are delocalized on both the terpyridine and the $DASP^+$. The lowest unoccupied

(58) Becke, A. D. J. *J. Chem. Phys.* **1993**, *98*, 5648–5652.
(59) Lee, C. T.; Yang, W. T.; Parr, R. G. *Phys. Rev. B* **1988**, *37*, 785–789.
(60) Rassolov, V. A.; Ratner, M. A.; Pople, J. A.; Redfern, P. C.; Curtiss, L. A. J. *Comput. Chem.* **2001**, *22*, 976–984.
(61) (a) Adamo, C.; Barone, V. *J. Chem. Phys.* **1999**, *110*, 6158–6170. (b) Ernzerhof, M.; Scuseria, G. E. *J. Chem. Phys.* **1999**, *110*, 5029–5036.
(62) Barone, V.; Polimeno, A. *Chem. Soc. Rev.* **2007**, *36*, 1724–1731.
(63) Jacquemin, D.; Perpete, E. A.; Ciofini, I.; Adamo, C. *Acc. Chem. Res.* **2009**, *42*, 326–334.

Table 4. Principal Computed Electronic Transitions (λ_{calc}; E) and Associated Oscillator Strength (f), along with Absorption Maxima for Simulated (λ_{sim}) Absorption Bands Together for the Ligands $\mathbf{L}_n$ with Corresponding Reliability Factors, R (in %)

compound	λ_{calc} [nm]	E [eV]	f	configuration (%)	$\lambda_{sim.}$ [nm]	R
$\mathbf{L_1}$	469	2.64	1.47	HOMO→LUMO (60) HOMO-1→LUMO (13)	470	3.2
$\mathbf{L_2}$	486	2.55	3.13	HOMO→LUMO+1 (24) HOMO-1→LUMO (22) HOMO-1→LUMO+1 (15) HOMO→LUMO (10)	485	−0.3
$\mathbf{L_3}$	482	2.57	2.95	HOMO-1→LUMO (20) HOMO-1→LUMO+1 (14) HOMO→LUMO (12) HOMO→LUMO+1 (24)	482	0.1

molecular orbital (LUMO) is a π^* centered on the $DASP^+$. In $\mathbf{L_2}$ and $\mathbf{L_3}$ a set of degenerate frontier orbitals (energy differences ≤0.0005 eV) centered on each $DASP^+$ were found both for the HOMOs and LUMOs. TDDFT was then performed at the same level of theory. Only singlet−singlet transitions, that is, spin-allowed transitions, have been taken into account. Moreover, only transitions with non-negligible oscillator strengths ($f \geq 0.04$) are reported and discussed. Computations were carried out to cover a spectral region up to 350 nm for all systems under investigation, that is, to span the whole UV−vis spectral domain. The first transition found for all three ligands is a $DASP^+$ centered charge transfer (ICT) band (Table 4). The bands maxima are calculated at 469, 486, and 482 nm for $\mathbf{L_1}$, $\mathbf{L_2}$, and $\mathbf{L_3}$, respectively. For comparison, Me-$DASP^+$ was also studied, and the first absorption band was found at 467 nm (2.66 eV, $f = 1.32$). Except for $\mathbf{L_1}$, these values are in very good agreement with the experimental ones (error less than 0.02 eV). The special case of $\mathbf{L_1}$ comes from the lack of proper modeling of its electronic properties as seen from the molecular orbital descriptions where a spurious contribution of the terpyridine moiety in the HOMO is found. Limits of TDDFT have notably been reported by Dreuw et al., who demonstrated that substantial errors can be obtained by this method for molecules with different subunits that can be involved in reciprocal electron transfers and no overlap between their orbitals.[64] In our case, the situation is slightly different as the failure comes from the deficiency to get an accurate description of the ground state. Despite this fact, it is noteworthy that the oscillator strength of the bands for $\mathbf{L_1}$−$\mathbf{L_3}$ is proportional to the number of absorbing chromophores ($f(\mathbf{L_2}) \approx f(\mathbf{L_3}) \approx 2 \times f(\mathbf{L_1})$).

The ruthenium complexes were optimized starting from the previously calculated structures of the various ligands and using the B3LYP functional with a double ξ quality LANL2 basis set and corresponding pseudopotential[65,66] without couteranions. In complexes **Ru-1**, **Ru-1′**, and **Ru-2** the two terpyridine ligands are planar (N−C−C−N dihedral angles ≤0.7°) and orthogonal to each other (a mean angle of 89.8° was calculated between the planes of the central pyridine of each ligand). The Ru−N bond lengths were found at 2.00 to 2.02 Å for the central pyridyls and 2.11 Å for the remaining bonds. These values are slightly longer than those found in crystal structures of $Ru(tpy)_2$ derivatives[67−69] (1.96−2.00 and 2.05−2.09 Å, respectively) but this fault is a known limitation of the B3LYP/LANL2DZ method when applied to this type of systems.[70] On the other hand, N−Ru−N angles are very similar to the crystal structure data. The phenyl ring is twisted out of the plane of the terpy as in the calculated ligands but this twist is slightly decreased in **Ru-1′** and **Ru-1** (32.5 and 31.5°, respectively) while in **Ru-2** it remains at 35°. The dimethylanilinyl-terpyridine ligand in **Ru-1′** has its own geometric features. The phenyl ring is coplanar with the amine (like in $DASP^+$) but the twist between the tpy and the phenyl ring is less marked (17.5°) which reflect the donor−acceptor nature of this ligand. The $DASP^+$ remains totally out of planes with the rest of the ligand (the angle between their mean plane and the phenyl rings are 85, 84, and 60° for **Ru-1′**, **Ru-2**, and **Ru-3**, respectively) and points in opposite directions in **Ru-2**. The calculated geometry for **Ru-3** matches a classical $Ru^{II}(bpy)_3$ complex with coplanar bipyridyl ligands (N−C−C−N dihedral angles of 1.8° and 1.7° for $\mathbf{L_3}$ and the two bpy, respectively) and are nearly perpendicular to each other (88°). Ru−N bond lengths are found at 2.10−2.11 Å which are slightly longer than those found in crystal structures (2.06−2.07 Å).[68−70] N−Ru−N angles are similar to crystal structures when nitrogen from two bipyridine moieties are involved, but they are different when one from $\mathbf{L_3}$ is involved. For example, the angle between nitrogen atoms opposite to each other from the ruthenium is found at 171.8° for two bipyridine (170.8−172.2° in the crystal structure) while it is 174.2° when one N from $\mathbf{L_3}$ is involved. Similarly, for nitrogen atoms on different ligands located roughly at 90° from each other, they make an angle of 95.7° between bipyridyl ligands and 88.9 or 97.4° when one N from $\mathbf{L_3}$ is involved (they range from 89.4 to 96.8° in the crystal structure). This might reflect the influence of the proximity of the two $DASP^+$ residues lying close to the ruthenium center. The two $DASP^+$ point in opposite direction and are perpendicular to the pyridyl moiety (88° calculated angle).

The electronic structure and excited states of the complexes were then calculated at a higher level of theory using PBE0 hybrid exchange correlation functional with the LANL2DZ basis set. Such a level of theory was proven to provide reliable results for spectroscopic properties of Ru complexes.[71] In all complexes, the first

(64) Dreuw, A.; Head-Gordon, M. *J. Am. Chem. Soc.* **2004**, *126*, 4007–4016.
(65) Dunning Jr., T. H.; Hay, P. J. In *Modern Theoretical Chemistry*; Schaefer, H. F.; III, Ed.; Plenum: New York, 1976; Vol. *3*, pp 1−28.
(66) Guillemoles, J.-F.; Barone, V.; Joubert, L.; Adamo, C. *J. Phys. Chem. A* **2002**, *106*, 11354–11360.
(67) Lashgari, K.; Kritikos, M.; Norrestam, R.; Norrby, T. *Acta Crystallogr., Sect. C* **1999**, *55*, 64–67.
(68) Craig, D. C.; Scudder, M. L.; McHale, W. A.; Goodwin, H. A. *Aust. J. Chem.* **1998**, *51*, 1131–1140.
(69) Pyo, S.; Perez-Cordero, E.; Bott, S. G.; Echegoyen, L. *Inorg. Chem.* **1999**, *38*, 3337–3343.
(70) Lundqvist, M. J.; Nilsing, M.; Lunell, S.; Akermark, B.; Persson, P. *J. Phys. Chem. B* **2006**, *110*, 20513–20525.
(71) (a) Ciofini, I.; Lainé, P. P.; Bedioui, F.; Adamo, C. *J. Am. Chem. Soc.* **2004**, *126*, 10763–10777. (b) Lainé, P. P.; Ciofini, I.; Ochsenbein, P.; Amouyal, E.; Adamo, C.; Bedioui, F. *Chem.—Eur. J.* **2005**, *11*, 3711–3727. (c) Ciofini, I.; Lainé, P. P.; Bedioui, F.; Daul, C. A.; Adamo, C. *C. R. Chim.* **2006**, *9*, 226–239. (d) Ciofini, I. *Theor. Chem. Acc.* **2006**, *116*, 219–231. (e) Lainé, P. P.; Loiseau, F.; Campagna, S.; Ciofini, I.; Adamo, C. *Inorg. Chem.* **2006**, *45*, 5538–5551.

Table 5. Selected Computed Electronic Transitions (λ_{calc}; *E*) and Associated Oscillator Strength (*f*), along with Absorption Maxima for Simulated (λ_{sim}) Absorption Bands Together for the Complexes **Ru-*n***, and Corresponding Reliability Factors, *R* (in %)

compound	λ_{calc}.[nm]	*E* [eV]	*f*	configuration (%)	λ_{sym} [nm]	*R*
Ru-1	479	2.59	3.72	HOMO-1→LUMO+7 (27), HOMO→LUMO+8 (27)	478	3.0
	446	2.78	0.11	HOMO-7→LUMO (32); HOMO-6→LUMO+1 (33)		
	409	3.03	0.15	HOMO-8→LUMO+2 (87)		
Ru-2	482	2.57	1.87	HOMO-2→LUMO+10 (12)	478	3.5
	481	2.58	3.11	HOMO-3→LUMO+10 (15)		
	472	2.63	2.80	HOMO→LUMO+10 (12)		
	410	3.02	0.09	HOMO-12→LUMO+2 (81)		
Ru-3	478	2.59	2.40	HOMO-1→LUMO+6 (32); HOMO→LUMO+5 (31)	472	4.8
	466	2.66	1.85	HOMO-1→LUMO+5 (30); HOMO→LUMO+6 (30)		
	397	3.12	0.05	HOMO-8→LUMO+2 (24); HOMO-7→LUMO+1 (20)		
	394	3.14	0.05	HOMO-8→LUMO+2 (19); HOMO-7→LUMO+1 (31)		
Ru-1′	623	1.99	0.55	HOMO-1→LUMO+2 (83)		
	477	2.60	1.67	HOMO→LUMO+4 (53)	474[a]	5.6
	463	2.68	0.23	HOMO-3→LUMO (30); HOMO-2→LUMO+1 (27)		
	419	2.96	0.10	HOMO-2→LUMO+1 (38)		

[a] Maximum of the main CT band centered on the $DASP^+$.

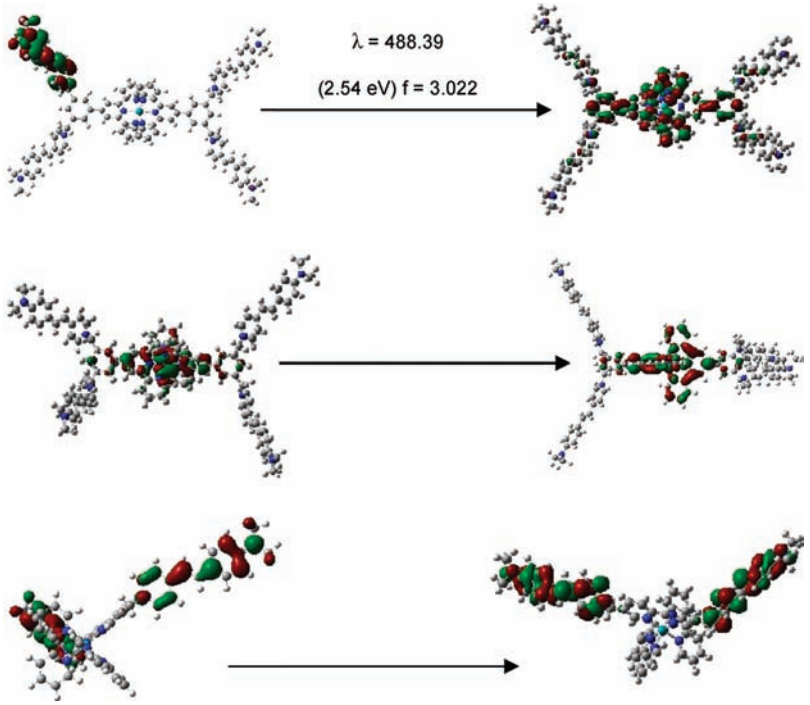

Figure 8. Dominant configuration of the electronic transition of charge transfer absorption of **Ru-2** (top), MLCT absorption of **Ru-2** (middle), and charge transfer absorption of **Ru-3** (bottom).

HOMOs are π ones centered on $DASP^+$ and the tpy-NMe_2 in **Ru-1′**. The metal centered d orbitals are lower in energy and are mixed with the pyridines' π cloud. The ordering of the LUMOs is also similar for all complexes. The first ones are π^* centered on the terpyridines or bipyridines while $DASP^+$ (or tpy-NMe_2 for **Ru-1′**) π^* ones are found at higher energy, contrariwise to the case of the corresponding ligands.

TDDFT calculations results are reported in Table 5. For complexes **Ru-1**−**3** the first computed electronic transitions are all intense $DASP^+$ charge transfer transitions. In those complexes made of several chromophores, several individual transitions, close in energy, are computed. They are found at 479 nm for **Ru-1**, between 472 and 482 nm (three transitions) for **Ru-2**, and at 466 and 478 nm for **Ru-3**. Then many MLCT bands of smaller intensity are found at lower energy, typically around 400 nm. Typical orbitals involved in those transitions are depicted in Figure 8.

Reconstructed spectra all yield a single band dominated by the *DASP* centered charge transfer with a maximum in fairly good agreement with the experimental data although the reliability factors are larger than for the ligands (Figure 9). This was not unexpected as it is known that in such type of approach, the errors are larger for inorganic dyes than for organic molecules.[60]

On the other hand, TDDFT calculations on complex **Ru-1′** give surprising results (Figure 9). Indeed, an ICT band on the tpy-NMe_2-Ru moiety is found at 623 nm while $DASP^+$ ICT and MLCT were calculated at higher energies (477 and 419 nm respectively). Hence the calculation grossly underestimates the energy of the first ICT while the other transitions agree well with experiment. The use of other basis sets did not improve this result. It is

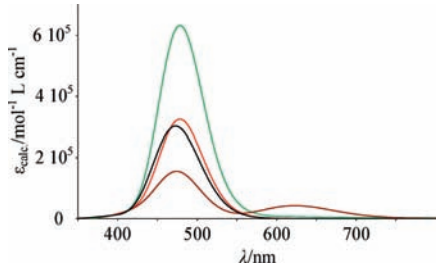

Figure 9. Theoretical absorption spectra from TDDFT calculations for Ru^{II} complexes. **Ru-1** (red line), **Ru-1′** (brown line), **Ru-2** (green line), **Ru-3** (black line).

Table 6. Nonlinear Optical Measurements Obtained by HLS

	L_1	Ru-1′	Ru-1	Zn-1	Ru-2	Ru-3
concentration (mol L^{-1})	5×10^{-3}	5×10^{-3}	10^{-3}	5×10^{-3}	10^{-3}	10^{-3}
β (10^{-30} esu)	330	340	630	370	610	750

The relative error on β values is ± 10%.

anticipated that the use of more a reliable approach using multireference perturbation theory (e.g., CASPT2) could lead to a better picture but the size of the molecule is a limit difficult to overcome in terms of calculation time.

Harmonic Light Scattering spectroscopy. The average hyperpolarizabilities of L_1 and of various Ru and Zn complexes are given in Table 6. The β value of L_1 is dominated by that of the $DASP^+$-like subunit *R*: for the pure Me-$DASP^+$ molecule measured at the same concentration as for L_1, $\beta_{DASP} = 270 \times 10^{-30}$ esu. Complexation of L_1 by ruthenium slightly increases the apparent β value, as β in **Ru-1′** is almost the same as for L_1. A superficial analysis would consider the influence of the **Ru-1′** complex core as negligible. However, according to previous studies evidencing significant β values for transition metal bipyridine complexes,[12] the apparent β value of **Ru-1′** could be described more adequately as the superimposition of 3 contributions, that is, β_{DASP}, β_{ICT}, and $\beta_{d\rightarrow\pi^*}$, corresponding to *DASP*, ICT, and d → π^* transitions, respectively. The β_{ICT} and $\beta_{d\rightarrow\pi^*}$ contributions to the β tensor may be either positive or negative with respect to that of β_{DASP}, but their relative contributions to the β tensor are opposite. At the present stage of this study we cannot identify the relative signs of β_{ICT} and $\beta_{d\rightarrow\pi^*}$ contributions with respect to that from β_{DASP}. The similar β values of L_1 and **Ru-1′** most probably arise from the (weak) contribution to β(**Ru-1′**) from the difference between β_{ICT} and $\beta_{d\rightarrow\pi^*}$.

On the contrary, the β value of **Ru-1** is almost twice higher than that of L_1. This increase can be due to the presence of two $DASP^+$-like molecules in the **Ru-1** structure. It has been shown before that the β value of a centrosymmetric collection of *N* nonlinear molecules varies as $\sqrt{N}$ when increasing *N* while the β value of a perfectly ordered noncentrosymmetric collection of *N* nonlinear molecules varies as *N* when increasing *N*.[49] Therefore, for two $DASP^+$ molecules, the β value is expected to increase by a $\sqrt{2}$ factor as compared to L_1 if the two $DASP^+$ units are oriented in a centrosymmetric manner within the **Ru-1** supramolecular unit. As the real β value is significantly higher than the expected 470×10^{-30} esu value expected from this simple model, the difference may be assigned to acentric order of the $DASP^+$ units within **Ru-1**. Therefore, the high β value of **Ru-1** is most probably due to the contributions of the two $DASP^+$ molecules ($2\,\beta_{DASP}$).

However, the NLO response of **Zn-1** is much lower than that of **Ru-1** and barely exceeds that of L_1. It must be pointed out that, contrarily to ruthenium complexes where d → π^* transitions significantly contribute to the nonlinearity, zinc complexes only involve ICT processes that may partially counterbalance the contribution from the two $DASP^+$ molecules. As a consequence, this would mean that the ICT contribution from the Zn^{2+} core complex is "negative" with respect to that of the $DASP^+$ molecules. Another possible cause of this lower β value could be due to a less ordered alignment of $DASP^+$ molecules as compared to **Ru-1**, but the reasons of such increase of disorder are still unclear.

In the case of **Ru-2**, the experimental β value is compatible with the model: its value is almost twice higher than that of L_1, with 4 $DASP^+$ molecules that are expected to be organized in a centrosymmetric manner within the complex. In this case the $DASP^+$ contribution dominates the NLO response, as already shown with **Ru-1′**. More surprisingly, a high β value is also reported for **Ru-3**, where only two $DASP^+$ molecules are present. In this case a partial dipolar order may influence the hyperpolarizability value, as the two $DASP^+$ units are attached to the same bipyridine ligand and may tend to align in the same direction. Therefore, these NLO measurements provide interesting information about the relative order of the $DASP^+$ units around the Ru core, although this aspect should be moderated by the role of the metal−ligand core as shown by comparing ruthenium and zinc complexes. The question of $DASP^+$ ordering in different transition metal complexes is not fully clarified at this stage and will require more detailed investigations in a future work.

Conclusion

A series of pro-ligands and metallic complexes based on chromophore-substituted bidentate and tridentate polypyridyl ligands have been synthesized and their electrochemical, linear (absorption and luminescence), and second order nonlinear (HLS) optical properties have been thoroughly investigated. Theoretical calculations have also been performed using DFT and TDDFT. A highly NLO active chromophore, namely, 4-(4-*N*,*N*-dimethylaminostyryl)-1-methyl pyridinium ($DASP^+$), exhibiting luminescence properties has been successfully covalently grafted to polypyridyl metal complexes, giving birth to a series of multifunctional metal complexes. The synthetic approach presented here allowed for the incorporation of up to four $DASP^+$ moieties in bis-terpyridine and tris-bipyridine derivative metal complexes and can be easily tuned to generate a variety of multifunctional compounds.

A good correlation of the measured and calculated absorption maxima has been observed for all complexes, and the ICT and the MLCT contributions in the overall band have been determined. Theoretical calculations highlighted the fact that for most of the complexes, the HOMOs are centered on the $DASP^+$ moiety whereas the LUMOs are localized on the ligand moiety (bipyridine or terpyridine). Photoluminescence experiments evidenced a quenching of luminescence because of intramolecular electron transfer between the

polypyridyl ruthenium fragment and the chromophore in all ruthenium complexes whereas no quenching was detected with zinc complexes. Nevertheless, a decisive result lies in the fact that despite the quenching observed, even the terpyridine-functionalized metal complexes exhibited detectable luminescence at room temperature. Finally, HLS measurements showed that both the *DASP*$^+$ moieties (and their relative ordering) and the metal-polypyridyl core need to be considered to explain the nonlinear optical properties of the metal complexes.

Acknowledgment. We thank the CNRS, C'NANO IdF, and the ANR "Jeunes Chercheuses et Jeunes Chercheurs" in the frame of AURUS program for financial supports. Aurore Boudet and Marie Huguenot, both students from the University of Versailles, are strongly acknowledged for their participation in the spectroscopic measurements. We thank Céline Fosse (Service de Spectrométrie de Masse, ENSCP Paris) for her contribution during the mass spectrometric analyses.

Supporting Information Available: Table of Cartesian coordinates of optimized geometries of ligands and metallic complexes; table of highest occupied and lowest unoccupied orbitals for ligands $\mathbf{L_1}$, $\mathbf{L_2}$, $\mathbf{L_3}$ and Me-*DASP*$^+$; figure of energy levels of the calculated molecular orbitals of ligands $\mathbf{L_1}$, $\mathbf{L_2}$, $\mathbf{L_3}$ and Me-*DASP*$^+$; figure of reconstructed spectra from TDDFT calculations for ligands $\mathbf{L_1}$, $\mathbf{L_2}$, $\mathbf{L_3}$ and Me-*DASP*$^+$; table of selected orbitals of complexes **Ru-1**, **Ru-1′**, **Ru-2** and **Ru-3**, figure of energy levels of the calculated molecular orbitals of complexes Ru-1, **Ru-1′**, **Ru-2**, and **Ru-3**, ^{1}H NMR spectra of $\mathbf{L_3}$ and **Ru-3** and ESI-MS spectra of $\mathbf{L_2}$ and **Ru-2**. This material is available free of charge via the Internet at http://pubs.acs.org.